Title

Low—Energy Metastable Ensemble—Involving Ostwald Ripening of Au Nanoclusters on Anatase TiO2(101) under Oxidizing Conditions

Journal

Journal of the American Chemical Society

ISSN

0002-7863

Authors

Liu, Qian-Yu
Chen, Dongxiao
Sautet, Philippe

Publication Date

2026-09-04

DOI

10.1021/jacs.6c15677

Low–Energy Metastable Ensemble–Involving Ostwald Ripening of Au Nanoclusters on Anatase TiO_2(101) under Oxidizing Conditions

Qian-Yu Liu [a], Dongxiao Chen [a], Philippe Sautet [a,b,c] *

[a] Department of Chemical and Biomolecular Engineering, University of California, Los Angeles, California 90095, United States

[b] Department of Chemistry and Biochemistry, University of California, Los Angeles, California 90095, USA

[c] California NanoSystems Institute, University of California, Los Angeles, California 90095, USA

* Email: sautet@ucla.edu

Abstract

Supported Au nanoclusters are highly effective catalysts but are susceptible to deactivation via sintering. While Ostwald ripening (OR) is a primary sintering mechanism, its atomic-scale pathways on the anatase TiO_2 surface remain poorly understood. Using neural network potential, we investigate the OR process of Au nanoclusters supported on TiO_2(101) under oxidizing conditions, identifying Au and AuO as the primary mobile species. A systematic Monomer Detachment Mapping (MDMAP) workflow is developed to efficiently sample the detachment landscape. Subsequent kinetic analysis reveals that low-energy metastable ensembles (LEMEs) serve as essential kinetic intermediates. By evaluating clusters with varying sizes and oxygen coverages, we identify interfacial oxygen as the key regulator of OR kinetics, where moderate oxidation promotes OR through charge stabilization and low Au-Au coordination, while excessive oxidation inhibits monomer detachment. This study provides a comprehensive atomistic perspective on Au nanocluster evolution, offering key insights into the rational design of stable supported catalysts.

1. Introduction

Supported metal nanoparticles are cornerstone catalysts in heterogeneous catalysis[1–6]. The nanoparticle size is a critical factor dictating the catalytic activity. For example, small Au nanoparticles (2~5 nm) have been demonstrated to exhibit excellent activity for low-temperature CO oxidation[7–10]. However, under realistic reaction conditions, particularly at elevated temperatures, these nanoparticles frequently undergo sintering, which leads to particle growth, loss of active surface area, and subsequent catalyst deactivation[11,12]. Sintering is generally governed by two primary mechanisms[12,13]: particle migration and coalescence (PMC), involving the mobility and merging of entire nanoparticles, and Ostwald ripening (OR), characterized by the detachment, diffusion, and re-incorporation of individual atoms or small molecular species. Among such supported metal catalysts, the Au/TiO_2 catalyst has attracted significant interest due to its exceptional performance in CO oxidation[14–19], propene epoxidation[20–23] and photocatalysis[24–26]. Nevertheless, the atomic-scale details of Au species detachment and diffusion on TiO_2, which are the fundamental steps of the OR process, remain elusive.

The sintering behavior of Au/TiO_2 has been extensively probed using transmission electron microscopy (TEM)[27,28] and scanning tunneling microscopy (STM)[29]. Although these in situ studies were typically conducted under low pressures (<1 mbar) over short timescales (up to several hours), both PMC and OR have been captured. Furthermore, the adsorbate-induced sintering[30,31] has been identified through ex situ TEM by comparing particle size distributions before and after exposure to various atmospheres (1 bar Ar, O_2, CO and mixed O_2+CO (O_2:CO=4:1))[28]. These findings suggest that O_2 and mixed CO+O_2 gas phase promote sintering under oxidizing conditions, resulting in significant particle growth (from 3 to 10 nm) within 48 h at 673 K on the anatase TiO_2(101) surface. Despite these insights, how oxidizing conditions specifically dictate the atomic-level OR mechanisms involving sub-nanometer mobile species remains poorly understood at the atomic level.

On the theoretical side, while the PMC process has been extensively studied via molecular dynamics (MD) simulations[32,33], the OR process remains less understood due to the complexity of its elementary steps, including monomer detachment and diffusion. To date, most theoretical investigations into OR have relied on simplified models, such as single adatoms on supports (e.g. Au_1/TiO_2)[27,34]. These models frequently overlook the critical roles of adsorbate effects[35–38] and charge-transfer interactions between larger nanoclusters and the monomer[39].

For instance, Yuan et al.[27] employed density functional theory (DFT) to study Au adatom diffusion on the anatase TiO_2(101) surface, reporting a diffusion barrier of merely 0.19 eV, which cannot explain the experimentally observed kinetics. Furthermore, the detachment step is rarely addressed due to the intricate structural transitions involved, which encompass not only the global minimum (GM) of the Au particle on the support but also a vast low-energy metastable ensemble (LEME)[40–47], particularly under high-temperature conditions.

In this work, we employed a neural network potential to explore the overall OR mechanism of Au nanoclusters on the anatase TiO_2(101) surface, Au/TiO_2(101), under oxidizing conditions. After characterizing the configurations and electronic states of stable AuO_x monomers, we established a systematic Monomer Detachment Mapping workflow to efficiently map the energetic landscape of monomer detachment, which reveals a set of candidate initial- and final-state structures and points to LEME configurations as key kinetic intermediates. Incorporating surface diffusion then allowed us to evaluate the ensemble kinetics through an apparent activation energy defined as the barrier of the optimal detachment-diffusion pathway, $\min[\max(E_{a,eff,i}^{det}, E_{a,eff,i}^{diff})]$, which confirms the decisive role of LEME over ground-state structures in dictating OR activity. Finally, by examining clusters of different sizes and oxygen contents, we revealed the promotional effect of adsorbed oxygen atoms: increasing oxygen coverage lowers the Au-Au coordination number and makes monomer detachment easier, with the nanocluster acting as an electronic reservoir for the accompanying charge transfer. Together, these results provide a comprehensive atomistic picture of oxidative nanocluster ripening.

2. Computational Methods

2.1. Monomer Detachment Mapping (MDMAP)

To uncover the OR mechanism of supported Au nanoclusters, we developed MDMAP, a structure-matching algorithm that maps final states (FSs) arising from monomer detachment onto their parent initial states (ISs). This method is motivated by the intrinsically fluxional nature of supported clusters[40–46], such that ripening pathways do not necessarily connect GM but may instead originate from the LEME. The scheme of MDMAP is shown in Figure 1. It starts with the exploration of the potential energy surface (PES) of the target Au_nO_m/TiO_2(101) interface as IS by the stochastic surface walking[48,49] method in combination with the neural network potential (SSW-NN). Based on the PES sampling, the unique IS GM and LEME structures are collected, with the LEME boundary set at ≤ 2.2 eV above the IS GM. This energy criterion represents the upper-bound activation barrier capable of achieving a TOF of 10^{-2} s^{-1} at 773 K under transition-state theory. For each minimum from the IS LEME and GM, each interfacial AuO_x motif is removed from the Au_nO_m cluster and a series of $Au_{n-1}O_{m-x}$ configurations on the support can be generated after structural relaxation. Based on the thermodynamics analysis of the AuO_x monomer adsorbed on the support, the AuO_x monomer is added in its most stable configuration to possible surface sites for each $Au_{n-1}O_{m-x}$ minimum. For example, the Au adatom is added to the bridge site (light-yellow circles with dashed outlines in the bottom right part of Figure 1) between two-coordinated oxygen atoms (O_{2c}) on TiO_2(101). After the structural relaxation, those structures with an additional AuO_x monomer adsorbed on the TiO_2 surface are filtered based on dual geometric criteria: a vanishing Au-Au coordination number (CN = 0) for the detached monomer and a minimum Au-Au separation distance (such as > 9 Å), and they combine to form the FS LEME and GM. In this way, we can map each FS ($Au_{n-1}O_{m-x}$+AuO_x) to the corresponding $Au_{n-1}O_{m-x}$, and thus to the corresponding IS (Au_nO_m). Leveraging the neural network potential, the MDMAP method effectively identifies the structural origins and dominant reaction pathways for monomer detachment from nanoclusters.

Conventional PES sampling methods designed to identify the GM are not well suited for exploring detached monomer-nanocluster configurations, because the intact nanocluster is always the most stable structure. Constrained PES sampling[50,51] can access detached monomer configurations by fixing selected coordinates, such as the monomer-nanocluster distance. However, the lowest-energy structures under such constraints still tend to

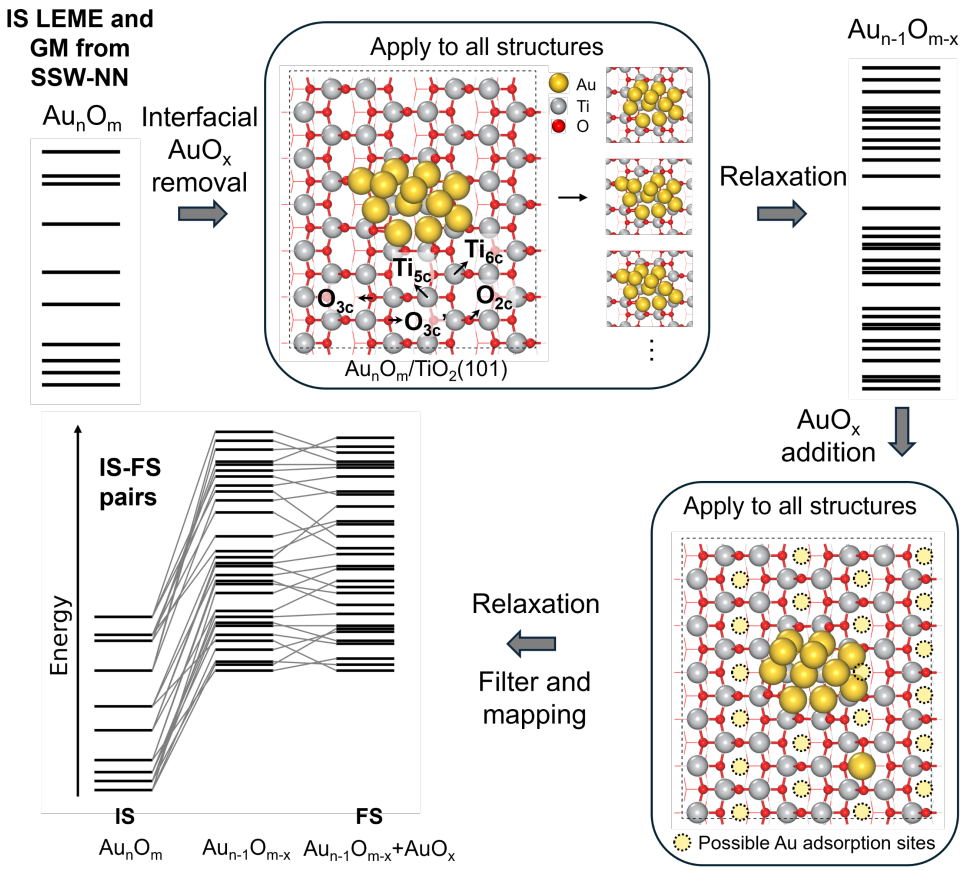

Figure 1. Schematic illustration of the MDMAP protocol for the monomer detachment process. The ISs of $Au_nO_m/TiO_2(101)$ systems are first identified using the SSW-NN method. The $Au_{n-1}O_{m-x}$ intermediates are derived by removing specific interfacial AuO_x species. The corresponding FSs ($Au_{n-1}O_{m-x}+AuO_x$) are constructed by placing the detached AuO_x monomers at their most energetically favorable adsorption sites on the $TiO_2(101)$. Representative sites for the Au adatom are indicated by the light-yellow circles with dashed outlines in the bottom-right panel. Each FS is systematically mapped to its parent $Au_{n-1}O_{m-x}$ intermediate and consequently, linked to the original IS. A top view of the $Au_{12}O_3/TiO_2(101)$ system in a (2×6) supercell illustrates the catalyst structure, with key surface atoms indexed: five-coordinated Ti (Ti_{5c}), six-coordinated Ti (Ti_{6c}), two-coordinated O (O_{2c}), and two distinct types of three-coordinated O (O_{3c} and O_{3c}').

place the monomer close to the cluster, making it difficult to efficiently sample configurations with large separations. In contrast, the MDMAP workflow not only samples detached monomer configurations in the presence of the nanocluster systematically, but also tracks the evolution of the detached species from the IS to the FS. This enables direct mapping of the detachment pathways and provides a more realistic description of monomer detachment in the nanocluster environment, offering insights beyond those obtained from isolated monomer models commonly used in previous theoretical studies[27,34].

2.2. Neural Network Potential

A ternary Au−Ti−O neural network potential (NN) in the many-body function corrected neural network (MBNN) architecture[52] was utilized for predicting the energy and force of the $Au/TiO_2(101)$ interfaces. The NN was trained in the large-scale atomic simulation with neural network potential (LASP) code (http://www.lasphub.com)[53].

The previously developed ternary NN[54] was further optimized to describe the interaction between AuO_x monomers and clusters on TiO_2(101). The updated dataset includes structures from Au and AuO diffusion pathways obtained via double-ended surface walking (DESW) method[55,56], post-detachment configurations at varying monomer-cluster separations generated by MDMAP, and structures sampled from MD trajectories, including enhanced MD trajectories for Au detachment from the cluster (See SI Section 1.1). These structures explicitly span equilibrium, thermally distorted, and reaction-coordinate-relevant geometries associated with monomer detachment. The final training data set consists of 13,044 structures in total (See Figure S1), where detachment-related configurations accounting for ~12%. The as-trained Au−Ti−O NN has three atomic feed-forward NN architectures using the hyperbolic tangent function as the activation function. Each atomic NN architecture contains five fully connected layers, with layer sizes of 299–128–80–80–9 for Au and Ti atoms, and 321–128–80–80–9 for O atoms. The input layer utilizes the power-type structure descriptor (PTSD)[57], and the entire model contains a total of 170,603 trainable parameters. Different from the high-dimensional NN architecture proposed by Behler and Parrinello[58,59], in which the output of the NN is a single atomic energy, the output in the MBNN potential is a vector utilized in many-body functions, 9 for the Au−Ti−O NN potential, including single-body, two-body, and three-body functions. The root-mean-square (RMS) errors of energy and force are 2.889 meV per atom and 0.116 eV $Å^{-1}$, respectively. The important low-energy structures from MDMAP were further examined by DFT calculations, and the benchmark results are shown in Figure S2, which showed that the energy RMS error is 1.44 meV per atom.

2.3. DFT Calculations

All DFT calculations were performed using the plane-wave Vienna Ab-initio Simulation Package (VASP)[60]. The electron−ion interaction was described by the projected-augmented wave (PAW) method[61], while the exchange-correlation functional utilized was the generalized gradient approximation Perdew−Burke−Ernzerhof (GGA-PBE) functional[62]. To correct for the self-interaction error of Ti 3d electrons, a Hubbard-like repulsion term was added using Dudarev's approach (PBE+U)[63], with U_{Ti} = U-J = 3.5 eV, determined using linear response[64]. The dDsC dispersion correction method[65] was used to account for van der Waals forces. Brillouin zone sampling was performed via the Monkhorst–Pack scheme. A k-point density of 25 reciprocal lattice units was used for bulk and (1×3) TiO_2(101) supercells. For larger (2×6) and (3×7) surface models (20.7 Å × 23.2 Å and 31.0 Å × 27.1 Å, respectively), only the Γ point was applied. The kinetic energy cutoff was 450 eV, and the criteria for convergence of the electron density and structure optimization were 5×10^{-6} eV for energy and 0.05 eV $Å^{-1}$ for forces. Spin polarization was considered in the DFT calculations for the structures with AuO_x monomers adsorbed on the TiO_2 surface.

It should be noted that all crucial minima predicted by NN were validated by single-point DFT calculations. Throughout this work, the NN potential is used solely to sample the configuration space and all energetic data and charge analyses reported here are subsequently recomputed at the DFT level without additional notation.

2.4. Modeling of Au/TiO_2(101) Interface

The Au/ TiO_2(101) interfacial model was constructed following our previous work[54]. The TiO_2(101) slab model consists of two TiO_2 layers, which was shown to be sufficient for relevant systems, with the bottom layer fixed at the bulk-truncated positions (see Table S1 for the influence of slab thickness). In all cases, the Au cluster and the top TiO_2 layer were fully relaxed. As shown in Figure 1, there are two types of Ti atom and three types of O atom on the perfect TiO_2(101) surface, including 0.50 monolayer (ML) of five-coordinated Ti (Ti_{5c}), 0.50 ML of six-coordinated Ti (Ti_{6c}), 0.50 ML of O coordinated with both Ti_{5c} and Ti_{6c} (O_{2c}), 0.25 ML of O coordinated with two Ti_{5c} and one Ti_{6c} (O_{3c}) and 0.25 ML of O coordinated with two Ti_{6c} and one Ti_{5c} (O_{3c}'). The TiO_2(101) surface was modeled using a conventional (1×1) surface unit cell defined by the surface vectors $\boldsymbol{u} = [10\bar{1}]$ and $\boldsymbol{v} = [010]$ (See Figure S3). We used a (1×3) supercell to study the isolated AuO_x monomer, while for the coupled system with the Au cluster, we used a (2×6) supercell for Au_{12} and a larger (3×7) supercell for Au_{30} and Au_{50} on the TiO_2(101) surface to accommodate different Au cluster sizes and minimize interactions

between periodic images. A vacuum region of at least 10 Å was introduced perpendicular to the slab, measured from the highest atom of the Au cluster to the bottom of the slab for the next periodic image. The adsorption free energy of the AuO_x monomer on the TiO_2 surface with a Au_nO_m cluster, G_{ad}, is calculated by Eq.1:

$$G_{ad} = [G(AuO_x + Au_nO_m/TiO_2) - G(Au_nO_m/TiO_2) - \mu_{Au} - x \cdot \mu_O] \quad \text{(Eq. 1)}$$

where $G(AuO_x+Au_nO_m/TiO_2)$ and $G(Au_nO_m/TiO_2)$ are the Gibbs free energy of the $AuO_x+Au_nO_m/TiO_2$ and Au_nO_m/TiO_2 interfaces, respectively. For the isolated AuO_x monomer (n=m=0), Eq.1 turns to Eq.2:

$$G_{ad} = [G(AuO_x/TiO_2) - G(TiO_2) - \mu_{Au} - x \cdot \mu_O] \quad \text{(Eq. 2)}$$

where $G(AuO_x/TiO_2)$ and $G(TiO_2)$ are the Gibbs free energy of the AuO_x/TiO_2 interface and the TiO_2 surface, respectively. μ_{Au} is the Au chemical potential from the face-centered cubic (fcc) bulk Au per atom. In this work, we consider μ_O to be the oxygen chemical potential from gas-phase O_2 under two conditions: (i) T=773 K and $P(O_2)=5\times10^{-7}$ bar (in situ TEM experimental condition[27]); and (ii) T=773 K and $P(O_2)=0.21$ bar (ambient pressure condition). In computing the free energy, we utilized the DFT total energy to approximate the free energy for solid states because the vibration entropy and the pV term contributions of solid phases are negligibly small; and we corrected the thermal and entropy contributions for gas phase O_2 molecule at finite temperatures. Zero-point energy correction was disregarded due to the insignificant influence on the system's energetics (See Table S2). A correction for the gas-phase O_2 (+0.40 eV) free energy is adopted to match the experimental enthalpy change for the gas-phase reaction ($H_2 + O_2 \rightarrow H_2O$).

The DESW method[55,56] in combination with constrained Broyden dimer (CBD) method[66,67] implemented in the LASP software was used to locate the transition state (TS) of AuO_x monomer detachment and diffusion on the TiO_2(101) surface based on an initial guess of IS and FS. All TSs were confirmed by the further extrapolation optimization to the correct ISs and FSs. All the pathways were computed by DFT.

2.5. Distance-Weighted Generalized Coordination Number (dGCN)

To correlate the structure of Au_nO_m clusters with their OR kinetics, we employ a smoothly-defined generalized coordination number (GCN)[68] to describe the local chemical environments of the Au clusters. Unlike the traditional discrete GCN, our formulation replaces the discrete counting of neighbors with a continuous function based on interatomic distances and atomic radii, which assigns lower weights to more distant neighbors. First, the local coordination environment of a single atom i is described by a smoothed coordination number, sCN_i, calculated using a sigmoid-type decay function:

$$sCN_i = \sum_{j \neq i} \frac{1}{1+exp(\frac{r_{ij}-r_c}{\sigma})} \quad \text{(Eq. 3)}$$

where r_{ij} is the interatomic distance between atom i and its neighbor j, and r_c represents the cutoff radius, defined as the sum of the atomic radii of atom i and its neighbor j plus 0.3 Å (for Au-Au pairs, r_c=2.88+0.3=3.18 Å). σ is the smoothing parameter that controls the steepness of the decay at the coordination shell boundary (σ=0.05 is used). Following the GCN framework, the distance-weighted GCN of a target atom i ($dGCN_i$) is determined by the average sCN of its neighbors, normalized by the ideal bulk coordination (CN_{max}=12 for fcc Au bulk):

$$dGCN_i = \sum_{j=1}^{n_i} \frac{sCN_j}{CN_{max}} \quad \text{(Eq. 4)}$$

3. Results

3.1. Geometry and Electronic State of AuO_x Monomer on the TiO_2(101)

To identify the key monomer involved in the OR process, we first employed SSW-NN to sample the configurational space of isolated AuO_x (x=0,1,2) monomers adsorbed on the TiO_2(101) surface. A total of 500 global optimization steps were performed for each composition to identify the most stable structures and relevant local minima. While these isolated systems represent the simplified models commonly adopted in previous studies, they serve as a foundation for our further analysis. Based on these low-energy monomer configurations,

we further constructed models where the AuO_x monomer is coupled with a parent Au cluster at separation distances exceeding 9 Å. By utilizing $Au_{12}O_3$ as a representative IS, these models more accurately capture the chemical environment encountered under realistic conditions following monomer detachment.

The geometries of eight representative AuO_x monomers at three compositions (x=0,1,2) are displayed in the middle of Figure 2a, which are described as follows:

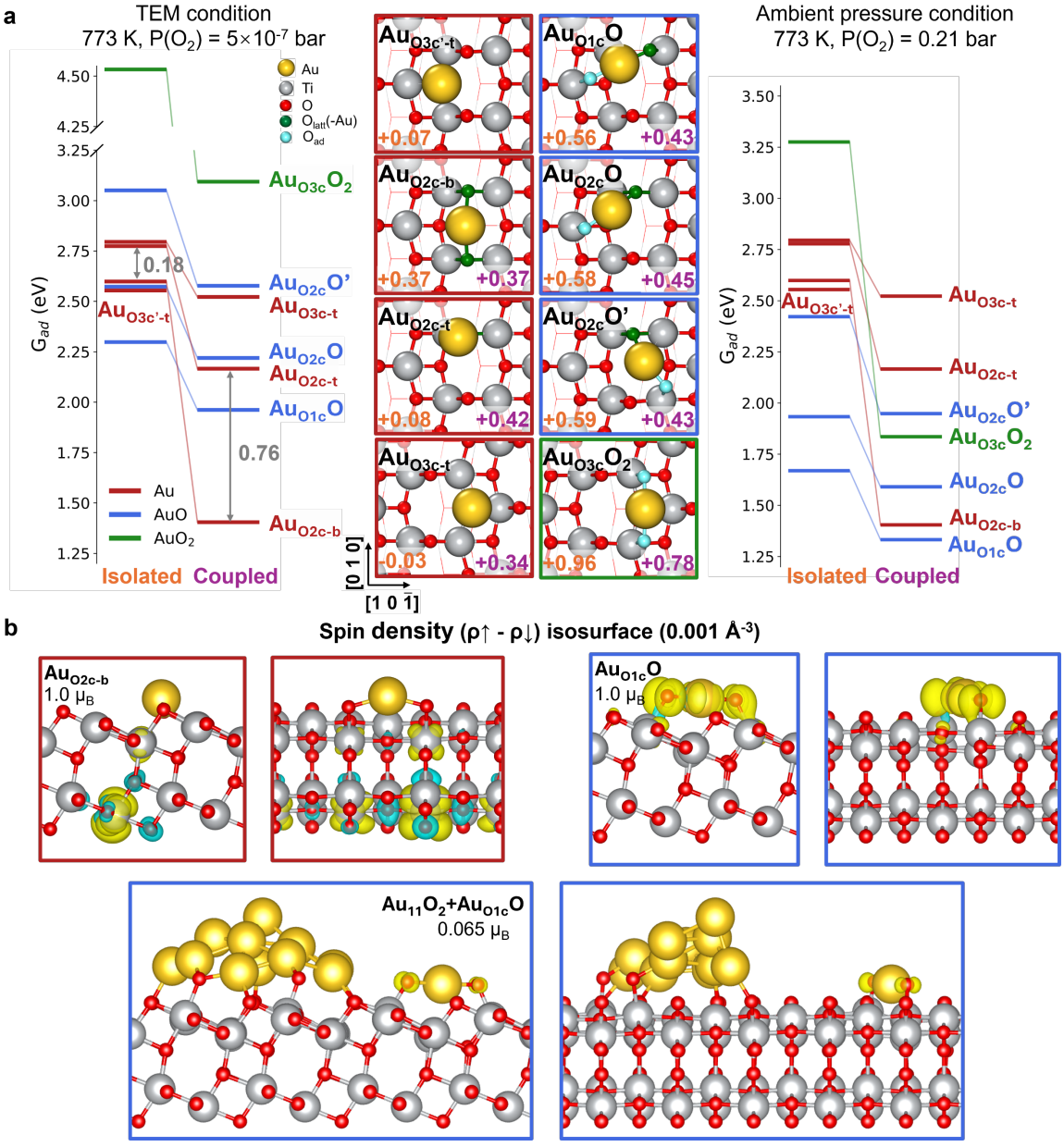

Figure 2. Thermodynamic stability and electronic states of AuO_x species in isolated and coupled systems. (a) Adsorption free energies (G_{ad}) and configurations of AuO_x (x=0,1,2) monomers under TEM and ambient pressure conditions. Net Bader charge of the Au atom in the monomer in isolated (orange) and coupled (purple) systems is labelled in the corner of each configuration. (b) Spin density distribution for $Au_{O2c\text{-}b}$ and $Au_{O1c}O$ in the isolated system, and $Au_{O1c}O$ in the coupled system ($Au_{11}O_2$+$Au_{O1c}O$). Yellow and blue isosurfaces represent spin-up and spin-down states, respectively (isosurface value=0.001 $Å^{-3}$).

(i) Au adatom: it tends to interact with one or two O atoms on the TiO_2(101) surface. Four distinct configurations are shown in Figure 2a, representing Au adatom adsorption at the top sites of O_{3c}' ($Au_{O3c'\text{-}t}$), O_{2c} ($Au_{O2c\text{-}t}$) and O_{3c} ($Au_{O3c\text{-}t}$) atoms, as well as the bridge site between two O_{2c} atoms ($Au_{O2c\text{-}b}$). The $Au_{O2c\text{-}b}$ exhibits a linear [O-Au-O] motif typically observed in the Au oxide phases[69–72]. In the isolated system, $Au_{O3c'\text{-}t}$ and $Au_{O2c\text{-}b}$ are identified as the two most stable configurations, with $Au_{O2c\text{-}b}$ being only 0.02 eV higher in energy. However, in the case where the Au adatom is placed together with a Au cluster on the TiO_2 (coupled system), $Au_{O3c'\text{-}t}$ is no longer a minimum even if the distance between adatom and cluster is significantly large (> 9 Å). Instead, $Au_{O2c\text{-}b}$ turns out to be the most stable configuration.

(ii) AuO monomer: its Au atom additionally coordinates with an O atom from the TiO_2(101) surface and its O atom adsorbs on the top site of a Ti_{5c}, forming a [O-Au-O] motif. The most stable AuO monomer configuration is linear, where the Au atom bonds with an O_{1c} ($Au_{O1c}O$ in Figure 2a). This structure originates from the cleavage of one Ti-O_{2c} bond. Less stable AuO configurations resemble $Au_{O1c}O$ but retain the O_{2c} unchanged, resulting in a deformed [O-Au-O] motif ($Au_{O2c}O$ and $Au_{O2c}O$' in Figure 2a).

(iii) AuO_2 monomer: its two oxygen atoms occupy the top sites of two neighboring Ti_{5c} atoms along [010] direction and its Au atom additionally coordinates to an O_{3c} atom from the TiO_2(101) surface ($Au_{O3c}O_2$ in Figure 2a). This monomer also exhibits a linear [O-Au-O] motif.

Figure 2a presents the adsorption free energies (G_{ad}) of these AuO_x monomers under two distinct oxidizing conditions. In general, Au (red) and AuO (blue) monomers are thermodynamically more favorable compared to AuO_2 (green). If the more realistic coupled monomer-cluster system is considered, thermodynamics indicate that $Au_{O2c\text{-}b}$ and $Au_{O1c}O$ are the key species for OR, serving as the GM under TEM and ambient pressure (773 K), respectively. Notably, $Au_{O1c}O$ and $Au_{O2c\text{-}b}$ emerge as the second-most stable configurations under these corresponding conditions. Under the TEM condition, the G_{ad} for $Au_{O2c\text{-}b}$ and $Au_{O1c}O$ are 1.40 and 1.96 eV (endothermic), respectively, while under the ambient pressure, their G_{ad} become nearly degenerate, with 1.33 eV for $Au_{O1c}O$ and 1.40 eV for $Au_{O2c\text{-}b}$.

Interestingly, there is a notable thermostability difference between monomers in isolated and coupled systems. Typically, AuO_x monomers are significantly stabilized when coupled with Au nanocluster systems due to monomer-cluster charge-transfer interactions, even at large separation. The differences in G_{ad} for the same monomer configuration between isolated and coupled systems range from -1.44 to -0.27 eV, indicating that these monomers are stabilized to varying degrees. Notably, the key configurations for the OR, $Au_{O2c\text{-}b}$ and $Au_{O1c}O$, are stabilized by 1.19 and 0.43 eV, respectively.

To elucidate the thermodynamic stability difference of the AuO_x monomers between isolated and coupled systems, we conducted Bader charge and spin density analysis. The net Bader charge for the Au atom in each monomer (Au_{mono}) calculated from isolated (orange) and coupled (purple) systems are labeled in the corner of each configuration in Figure 2a. In the isolated system, the Au adatom atom coordinated with only one O atom from the TiO_2 surface ($Au_{O3c'\text{-}t}$, $Au_{O2c\text{-}t}$ and $Au_{O3c\text{-}t}$) exhibits net Bader charge of nearly zero, suggesting a neutral Au^0 state. Conversely, isolated $Au_{O2c\text{-}b}$ adatom coordinated with two surface O atoms shows net Bader charge of +0.37 $|e^-|$, consistent with the Au^+ oxidation state. These findings are corroborated by spin density analysis (Figure 2b and Figure S5), which reveals that spin density is primarily localized on the Au adatom in isolated $Au_{O3c'\text{-}t}$, $Au_{O2c\text{-}t}$ and $Au_{O3c\text{-}t}$ systems, while it is distributed to the TiO_2 support in isolated $Au_{O2c\text{-}b}$ system. The isolated AuO monomers have +0.56 ~ +0.59 $|e^-|$ net Bader charge for Au_{mono} atom, with the localized spin density around the monomer (Figure 2b and Figure S5), suggesting a Au^{2+} oxidation state. Notably, despite varying oxidation states, the total magnetic moment for each isolated Au and AuO systems remains 1.00 μ_B. In contrast, the isolated $Au_{O3c}O_2$ exhibits a more pronounced positive Bader charge (+0.96 $|e^-|$) for the Au_{mono} atom and a larger total magnetic moment of 2.88 μ_B (Figure S5).

In contrast, when the monomer is coupled with the Au cluster, its electronic state undergoes a significant transformation, characterized by a markedly decreased magnetic moment due to charge-transfer interactions

(Figure 2b and Figure S6). The Au cluster serves as an electron reservoir capable of donating or accepting electrons to stabilize the monomer. For example, upon the detachment of one Au atom forming $Au_{O2c\text{-}b}$, the net Bader charge of the nanocluster shifts from +0.15 ($Au_{12}O_3$) to -0.26 $|e^-|$ ($Au_{11}O_3$), accompanied by the formation of a positively charged $Au_{O2c\text{-}b}$ adatom (+0.37 $|e^-|$). Similarly, in the case of $Au_{O1c}O$ detachment, the cluster donates electrons to the monomer (-0.40 $|e^-|$), with its own positive charge increasing from +0.15 ($Au_{12}O_3$) to +0.52 $|e^-|$ ($Au_{11}O_2$). The resulting magnetic moment is only 0.065 μ_B, much lower than that of the isolated system (1.00 μ_B), as further evidenced by the reduced spin density ($Au_{11}O_2$+$Au_{O1c}O$ vs. $Au_{O1c}O$) in Figure 2b. This long-range charge-transfer interaction is uniquely captured in the coupled system and is essential for an accurate description of the OR mechanism. Conversely, isolated models neglect these interactions, which may lead to an erroneous characterization of the ripening process. For example, previous studies[27] reported a very low barrier (0.19 eV) for $Au_{O2c\text{-}b}$ diffusion via the TS of the $Au_{O2c\text{-}t}$ configuration based on an isolated model. While this is consistent with the thermodynamic differences in the isolated system (0.18 eV in Figure 2a), our results reveal that the energy gap increases significantly to 0.76 eV when the cluster-monomer coupling is explicitly considered. This long-range charge-transfer interaction also set challenges for machine learning potentials (MLPs)[73] using local structural descriptors in the input layer and care should be applied when studying OR with such MLPs, since the energy of the coupled adatom-cluster system could be highly inaccurate. In our case, good accuracy is obtained by explicitly including coupled adatom-cluster systems in the training set, and all final energies are nevertheless validated through DFT recalculation.

3.2. MDMAP of Au and AuO Detachment

With the knowledge of the thermodynamics of AuO_x monomers, we performed MDMAP to study the detachment process in OR. Two specific monomers, Au and AuO, were selected for the detachment study due to the superior stability of $Au_{O2c\text{-}b}$ and $Au_{O1c}O$ configurations under both TEM and ambient pressure conditions (Figure 2a). The energy minima identified by the SSW-NN method in our previous work[54] served as the input for the ISs. To generate the corresponding FSs, the interfacial AuO_x motif was removed, and an Au adatom or AuO monomer was subsequently placed on the TiO_2(101) surface in accordance with its stable configuration ($Au_{O2c\text{-}b}$ or $Au_{O1c}O$). All potential adsorption sites for these monomers were considered. Finally, the FSs were filtered and collected based on the criteria mentioned in Section 2.1.

Since small particles are thermodynamically prone to monomer detachment, we first focus on this process using a small Au_{12} cluster. As reported in our previous work[54], two types of Au_nO_m/TiO_2(101) interfaces form as the adsorbed O content increases: Type (i), which forms during initial oxygen addition, with all O atoms adsorbed on Ti sites near the Au cluster; and Type (ii), which emerges upon further oxygen incorporation, featuring at least one O atom at an Au_3 hollow site. We selected $Au_{12}O_3/TiO_2$(101) as the representative model because, with its intermediate oxygen coverage, both interface types coexist within the ensemble. Using this system, we first establish the detailed OR mechanism, and the effects of cluster size and oxygen content are then examined systematically in Section 4. We begin with the MDMAP results for $Au_{12}O_3$. Starting from 356 $Au_{12}O_3$ IS configurations, we generated over 2500 $Au_{11}O_3$ or $Au_{11}O_2$ intermediate states and finally collected approximately 13,000 FSs (Au+$Au_{11}O_3$ or AuO+$Au_{11}O_2$). Figure 3a and 3b show the NN-calculated energy diagrams for the detachment of Au and AuO monomers, where the y-axis represents the energy relative to the IS GM (details are shown in SI Section 4.1). The positive energies of the FSs confirm the endothermic nature of the detachment process.

For clarity, Figure 3a and 3b display only the most stable FSs among those with a monomer-nanocluster separation exceeding 9.0 Å for each low-energy intermediate state. The detached monomers in these structures are denoted as Au_{far} and AuO_{far}. Detailed diagrams including all stable FSs without distance constraints are provided in Figure S7, revealing that the most stable adsorption sites for the Au and AuO monomers are located adjacent to the nanocluster (See Figure S8 and S9). For example, both Au and AuO monomers form a [O-Au-O]

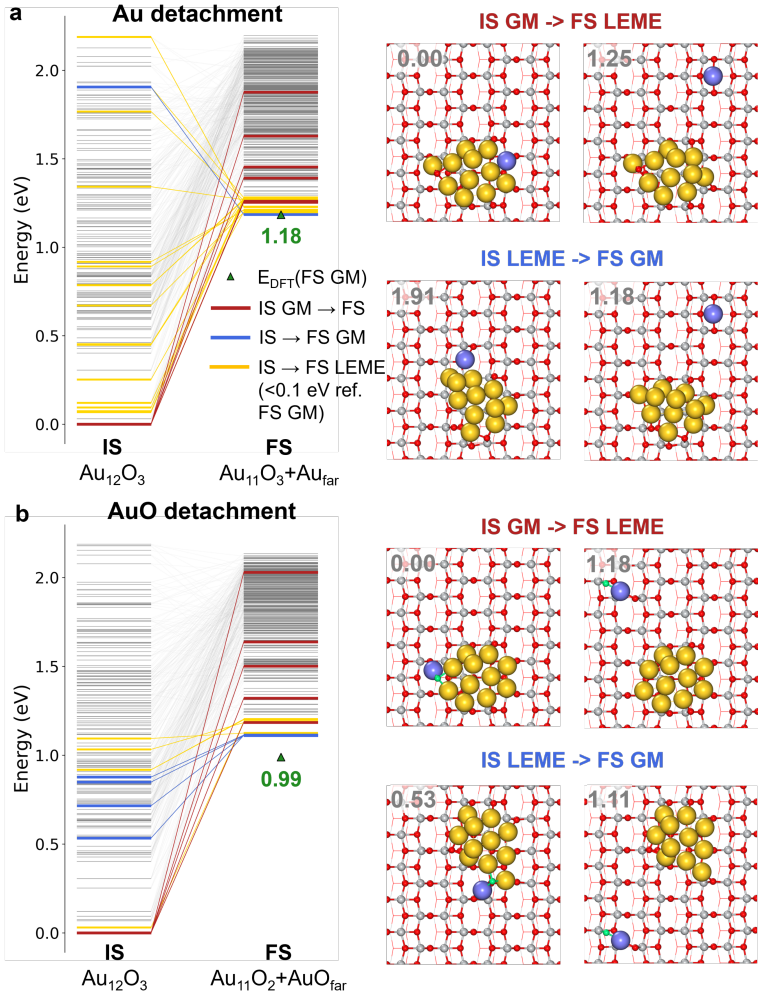

Figure 3. MDMAP for Au and AuO detachment from an $Au_{12}O_3$ cluster on the TiO_2(101) surface. (a-b) Energy profiles for (a) Au and (b) AuO detachment. For clarity, only the ISs (Au_nO_m) and FSs ($Au_{n-1}O_{m-x}$+AuO_x) are shown, with the intermediate states ($Au_{n-1}O_{m-x}$) omitted. In the FS section, only the lowest-energy FS among those with a monomer-nanocluster separation exceeding 9.0 Å is presented for each low-energy intermediate state. The detached monomers in these structures are denoted as Au_{far} and AuO_{far}. Red, blue, and yellow lines indicate the IS-FS pathways involving the IS GM to FS, IS to FS GM and IS to FS LEME (with energy ≤0.1 eV referenced to the FS GM), respectively. Representative pathways involving the IS and FS GM are displayed in the right panel, with detached Au and O atoms highlighted in blue and green, respectively. The corresponding energies are labeled in the upper-left corner of each structure.

motif where one O atom bonds with the Au cluster while the other originates from the O_{2c} of the TiO_2(101) surface. Our findings indicate that the diffusion of a monomer from a proximal site to a distal site is endothermic, with NN-calculated energies increasing from 0.40 to 1.18 eV for Au, and from 0.29 to 1.11 eV for AuO. The DFT-validated energies for the FS GMs at separation exceeding 9.0 Å, marked by triangles in Figures 3a and 3b, are 1.18 and 0.99 eV for Au and AuO, respectively. These results align with our NN predictions, suggesting that $Au_{11}O_2$+AuO is slightly more stable than $Au_{11}O_3$+Au and confirming the good accuracy of our NN potential.

Key IS-FS pairs are highlighted in Figure 3a and 3b, where red, blue and yellow lines represent the IS-FS mapping pathways involving the IS GM to FS, IS to FS GM and IS to FS LEME (with energy ≤0.1 eV referenced

to the FS GM), respectively. The right panel of Figure 3a and 3b illustrate representative IS-FS pairs involving IS GM and FS GM, while additional IS-FS pairs involving other low-energy FSs are provided in Figure S10 and S11. Notably, our MDMAP reveals that the IS GM does not necessarily evolve into the FS GM during OR. Instead, the LEME configurations for both the IS and FS play a critical role in the monomer detachment process. For instance, during the Au detachment, the IS GM can transition into six possible FS LEME configurations (red lines in Figure 3a) with energies ranging from 1.25 to 1.88 eV. The most stable FS LEME structure derived from the IS GM involves the detachment of an interfacial Au atom (blue sphere in Figure 3a) initially coordinated to three Au atoms and one surface O_{2c} atom. Conversely, the FS GM for Au detachment originates from an IS LEME with a markedly high energy of 1.91 eV (blue line in Figure 3a). In this pathway, an interfacial Au atom coordinated to two Au atoms and one O_{2c} atom detaches, accompanied by a slight counterclockwise rotation of the nanocluster to form a new interfacial Au-O_{2c} bond.

Similar behavior is observed for AuO detachment, where the IS GM transforms into various FS LEME structures across a broad energy range (1.18~2.03 eV, red lines in Figure 3b). The FS GM can be generated from four distinct IS LEME structures (0.53~0.88 eV, blue lines in Figure 3b), the most energetically favorable of which is depicted in Figure 3b. These FS structures result from the detachment of interfacial AuO species from low-energy ISs, where the Au atom is coordinated to two O atoms: one bonded to three Au atoms (O(-Au_3)) and another being a surface O_{2c} from TiO_2(101).

Based on the MDMAP diagrams in Figure 3a and 3b, we observed that certain IS LEME structures can lead to more stable FSs than the IS GM. Thermodynamically, the overall energy cost of the detachment process is defined by the higher energy level between the IS and the FS (max(E_{IS}, E_{FS})). The yellow lines in Figure 3a and 3b indicate that certain FS LEME structures, whose thermodynamic stability lies between that of the FS GM and the most stable FS LEME derived from the IS GM (i.e., the yellow bars between the blue bar and the lowest red bar in the FS region), exhibit a lower overall energy cost compared to the FS from the IS GM. Furthermore, our results suggest that Au or AuO detachment is thermodynamically less favorable for certain IS LEME structures, as they lead to significantly less stable FSs despite their own low initial energies (black bars in the IS region). Consequently, we propose that OR preferentially proceeds via low-energy IS-FS pairs where neither state is necessarily the GM, i.e. those minimizing max(E_{IS}, E_{FS}), thereby minimizing the overall thermodynamic energy cost.

3.3. Overall Mechanism of Ostwald Ripening via Au and AuO Monomers

The thermodynamic analysis above identifies which IS-FS pairs are energetically preferred, but not the kinetic feasibility of each elementary step. To resolve this, we investigated the reaction pathways for the detachment and surface diffusion of two monomer species, Au and AuO. Guided by the thermodynamic criterion introduced above, min[max(E_{IS}, E_{FS})], we selected two $Au_{12}O_3/TiO_2$(101) interfacial structures with the lowest overall energy cost for forming Au_{far}+$Au_{11}O_3$ and AuO_{far}+$Au_{11}O_2$ as representative models (Figures S10 and S11). These two models are chosen to isolate the intrinsic kinetics of the detachment and diffusion steps separately, and do not necessarily correspond to the lowest overall kinetic pathway. Other structures were also computed (Figure S12-S21, Table S3 and S4), but Figure 4a mainly focuses on these two representative models. Since monomer adsorption at distal sites is significantly more endothermic, we examined the surface diffusion of a monomer positioned far from the parent cluster (minimum Au–Au distance > 9.0 Å) to evaluate the overall kinetic barrier for the ripening process.

The reaction energy profiles for detachment and diffusion are shown in Figure 4a, with energies referenced to the IS GM. For each elementary process we distinguish two barriers: an intrinsic barrier (E_a), referenced to the local minimum from which the step departs — the IS LEME for detachment, or the FS LEME (detached

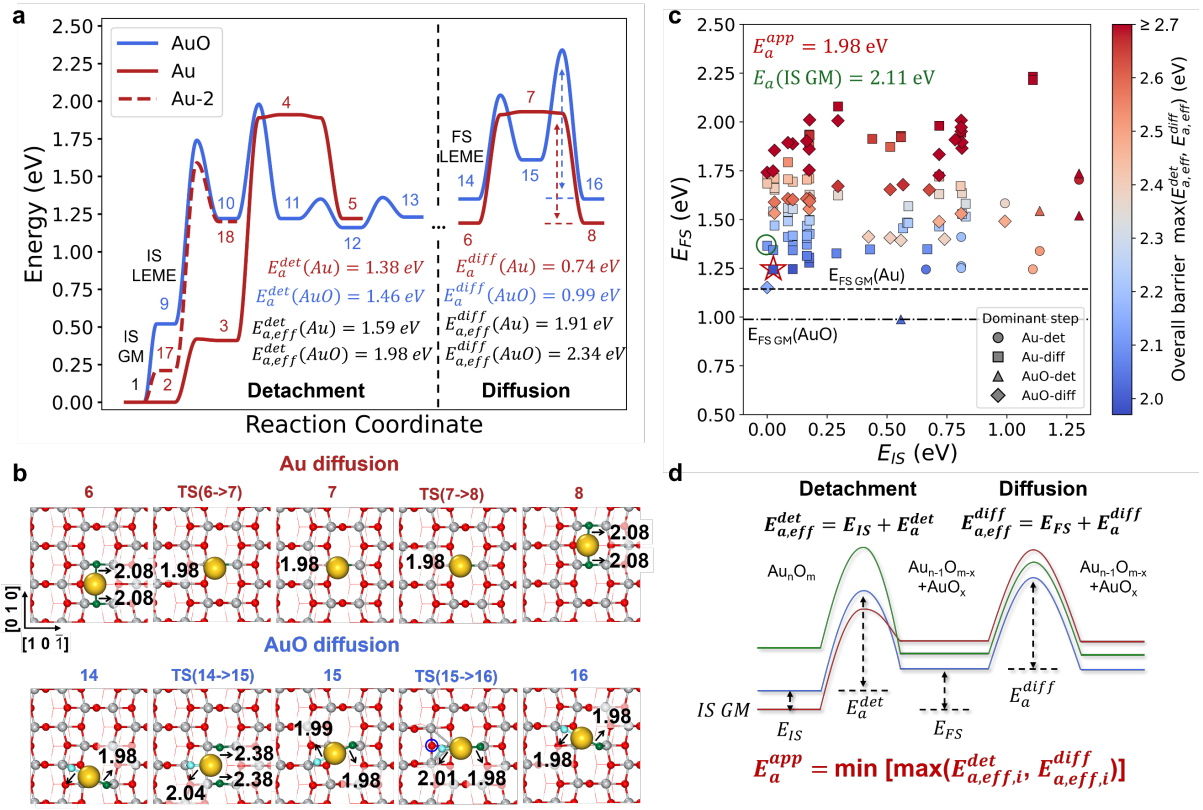

Figure 4. Mechanism of Au and AuO detachment from $Au_{12}O_3$ on TiO_2(101) and diffusion. (a) Reaction energy profiles for the detachment and surface diffusion of Au (red) and AuO (blue) on TiO_2(101). (b) Structural snapshots of the diffusion pathways for Au and AuO, with key Au-O distances highlighted. Surface lattice oxygen and adsorbed oxygen atoms are labeled in green and blue, respectively. For clarity, only the local surface environment surrounding the monomer is shown and the remaining cluster, while present, is not shown. (c) IS-FS map of the OR overall barrier for $Au_{12}O_3$. Each point is placed at the energies (E_{IS}, E_{FS}), the color indicates the overall barrier, while the symbols indicate the kinetically dominant step for each IS-FS pair. The energies of the FS GM for Au and AuO detachment are indicated by the dashed and dash-dotted lines, respectively. The lowest-energy pathway and the pathway via the IS GM are denoted by a red star and a green circle, respectively. (d) Determination of the apparent activation energy under the condition that cluster isomerization is faster than monomer detachment but slower than monomer diffusion.

monomer) for diffusion — and an effective barrier ($E_{a,eff}$), referenced to the IS GM, which additionally includes the energy cost of reaching that local minimum. The two coincide when the departing state is the IS GM, and $E_{a,eff} \geq E_a$ in general.

For detachment, the intrinsic barrier (E_a^{det}) spans 1-2 eV across configurations, while the effective barrier ($E_{a,eff}^{det}$) is correspondingly equal or larger (Table S3). Among all computed pathways, the lowest effective barriers are 1.59 eV for Au and 1.98 eV for AuO (red dashed and blue solid lines in Figure 4a), corresponding to intrinsic barriers of 1.38 and 1.46 eV, respectively. Both barriers are strongly correlated with the IS structure and the local chemical environment of the detaching monomer: detachment is more favorable for low-coordinated Au atoms and when the residual cluster retains a compact, highly coordinated core (higher Au–Au dGCN). The full analysis is provided in the SI (Figures S12-S15 and Table S3). Overall, detachment is endothermic, and AuO typically exhibits a higher effective barrier than Au.

For diffusion, the intrinsic barrier (E_a^{diff}) is largely independent of cluster size and O content for AuO (~0.99 eV), whereas for Au it depends on whether the residual cluster carries adsorbed O (O_{ad}): 0.74 eV when the cluster is O-adsorbed and only 0.19 eV for a bare Au cluster (Table S4). This arises because the O_{ad} atoms introduce low-energy vacant states between the Fermi level and the TiO_2 conduction band minimum (Figure S22), allowing Au_nO_m (m>0) clusters to act as charge reservoirs that accept the electrons released upon Au detachment. For a bare Au cluster, by contrast, detachment donates electrons to the TiO_2 substrate, as for the isolated system (Figure 2a), a situation which is less energetically stabilizing and corresponds to a lower E_a^{diff}. The representative models in Figure 4a correspond to the O-adsorbed case, for which the intrinsic diffusion barrier of the detached adatom is 0.74 eV for Au and 0.99 eV for AuO, whereas the effective barrier referenced to the IS GM ($E_{a,eff}^{diff}$, 1.91 eV for Au and 2.34 eV for AuO) is dominated by the endothermicity of the detachment step.

Regarding the Au diffusion mechanism (Figure 4b), the $Au_{O2c\text{-}b}$ monomer (state 6) traverses the surface O_{2c} atom along the [010] direction via an $Au_{O2c\text{-}t}$ intermediate (state 7) before returning to the $Au_{O2c\text{-}b}$ configuration (state 8). This process involves energy barrier of 0.74 eV (TS(6->7) and TS(7->8)). The Au-O bond length, initially 2.08 Å in $Au_{O2c\text{-}b}$, decreases to 1.98 Å in TS(6->7), $Au_{O2c\text{-}t}$ intermediate (state 7) and TS(7->8). The energy difference between states $Au_{O2c\text{-}t}$ and $Au_{O2c\text{-}b}$ is 0.74 eV, which is consistent with the thermodynamics results in Figure 2a. An alternative diffusion pathway via the $Au_{O3c\text{-}t}$ intermediate along $[10\bar{1}]$ direction was also investigated but was found to have a higher intrinsic barrier (1.12 eV in Figure S23). Our calculations indicate that anisotropic Au migration on TiO_2(101) is enthalpically favored, as diffusion along the [010] direction exhibits a lower activation barrier. However, under operational reaction conditions, especially at elevated temperatures, entropic contributions and enhanced surface mobility may diminish this energetic preference. We recall that the Au diffusion mechanism is calculated by DFT in the presence of the remaining $Au_{12}O_3$ cluster on the TiO_2(101), at a separation of at least 9 Å, which is critical for a correct description.

The diffusion of AuO initiates from the $Au_{O1c}O$ configuration (state 14), where the AuO monomer adopts a linear [O-Au-O] configuration characterized by symmetric Au-O bond lengths of 1.98 Å. In TS(14->15), the Au atom migrates along the [010] direction to a position between two O_{2c} atoms. While the oxygen atom derived from the TiO_2 substrate remains surface-bound, the Au atom maintains equal Au-O_{2c} distances of 2.38 Å. This transition involves an activation barrier of 0.69 eV, with the Au-O bond length within the monomer being 2.04 Å. Subsequently, the Au atom bonds with another O_{2c} atom, restoring the $Au_{O1c}O$ configuration in state 15. The subsequent diffusion step, involving the migration of the O atom in $Au_{O1c}O$ (state 15) between Ti_{5c} sites, represents the rate-determining step with a barrier of 0.73 eV (TS(15->16)). In this TS, both the Au and O atoms of the monomer are coordinated to two Ti atoms (one Ti_{5c} and one Ti_{6c}). Notably, the Ti_{6c} atom becomes five-fold coordinated due to the cleavage of a Ti_{6c}-O_{2c} bond during the formation of the $Au_{O1c}O$ species. Meanwhile, the O_{3c} atom beneath the monomer on the TiO_2(101) surface is displaced downward by 1.17 Å (highlighted by the blue circle in TS(15->16)). The Au-O distances for the AuO monomer and Au-O_{1c} are 2.01 and 1.98 Å, respectively.

Having characterized the two steps separately, we combined them to estimate the overall barrier for each IS-FS pair. Our estimate for the supported Au clusters gives the cluster isomerization barrier at ~1 eV (See Figure S25-S28), comparable to values reported for Pt clusters on Al_2O_3[74,75]. This makes isomerization faster than detachment (E_a^{det} = 1-2 eV) but slower than diffusion (E_a^{diff} = 0.19-0.99 eV). Isomerization can therefore interconvert configurations before detachment, but not before diffusion. The overall barrier of a pathway is thus set by the highest of its detachment and diffusion effective barriers, $\max(E_{a,eff,i}^{det}, E_{a,eff,i}^{diff})$. The apparent activation energy (E_a^{app}) of the ensemble is then the smallest $\max(E_{a,eff,i}^{det}, E_{a,eff,i}^{diff})$ over all pathways, $E_a^{app} = \min[\max(E_{a,eff,i}^{det}, E_{a,eff,i}^{diff})]$ (referenced to the IS GM shown in Figure 4d), that is, the barrier of the kinetically optimal pathway. This is the kinetic analogue of the thermodynamic criterion $\min[\max(E_{IS}, E_{FS})]$ used earlier. The other two

isomerization rate regimes, where isomerization is faster or slower than both detachment and diffusion, are discussed in the SI Section 6.2.

To evaluate the overall OR kinetics on $Au_{12}O_3/TiO_2(101)$, we performed a kinetic ensemble analysis over all IS-FS pairs identified by MDMAP. For each pair, we considered two reaction routes comprising four elementary processes: Au and AuO detachment and subsequent diffusion. As shown in Figure 4d, the effective barrier of each step, referenced to the IS GM, is defined as:

$$E_{a,eff}^{det} = E_{IS} + E_a^{det} \quad \text{(Eq. 5)}$$

$$E_{a,eff}^{diff} = E_{FS} + E_a^{diff} \quad \text{(Eq. 6)}$$

where E_{IS} and E_{FS} are the DFT single-point energies of the IS and FS, and E_a^{det} and E_a^{diff} are the intrinsic detachment and diffusion barriers from DFT. E_a^{diff} is essentially invariant for AuO (0.99 eV) and, for the O-adsorbed $Au_{12}O_3$ system considered here, is 0.74 eV for Au (Table S4). The E_a^{det} spans 1-2 eV depending on on configuration (Table S3). Here, for each species we adopted a single value taken from the pathway with the lowest effective barrier E_a^{det} = 1.38 eV for Au and 1.46 eV for AuO. The overall OR barriers for low-energy IS-FS pairs are shown in Figure 4c. Varying E_a^{det} over the 1-2 eV range for both Au and AuO does not qualitatively change the conclusions (SI Section 6.4).

Figure 4c shows as a color code the overall barrier ($\max(E_{a,eff}^{det}, E_{a,eff}^{diff})$) for each IS-FS pair, represented on the 2D graph by the energies (E_{IS} and E_{FS}), while the symbols indicate the rate-limiting step (Au or AuO detachment or diffusion). To keep the DFT workload tractable, we evaluated only the low-energy IS and FS structures selected by a Boltzmann-weighted screening (details in SI Section 6.3), which yields 115 pairs within E_{IS} < 1.35 eV and E_{FS} < 2.50 eV (72 for Au and 43 for AuO). The globally optimal pathway, which minimizes $\max(E_{a,eff}^{det}, E_{a,eff}^{diff})$, is highlighted (red star).

The map reveals two governing trends. First, the optimal pathway proceeds through IS or FS LEME rather than through the GM. The lowest-barrier pathway passes through an IS LEME (E_{IS}=0.03 eV) and an FS LEME (E_{FS}=1.24 eV) with an overall barrier of 1.98 eV, whereas the pathway through the IS GM (green circle, E_{IS}=0, E_{FS}=1.37 eV) is higher at 2.11 eV. The difference originates from the FS: our MDMAP results show that the FS derived from the IS GM lies higher in energy than those accessible from IS LEME, so it incurs a larger overall diffusion barrier ($E_{FS}+E_a^{diff}$). This highlights the decisive role of LEME structures in dictating OR activity. Conversely, pathways starting from high-energy IS structures that could thermodynamically yield low-energy FSs are kinetically blocked by their large detachment barriers. For instance, formation of the Au adatom FS GM from the IS at E_{IS}=1.91 eV (Figure 3a, blue line) is strongly disfavored.

Second, the low-energy pathways cluster in the low-E_{IS} and low-E_{FS} region, where they are predominantly diffusion-limited. Because the detachment step is highly endothermic ($E_{FS\ GM}$(Au)=1.18 and $E_{FS\ GM}$(AuO)=0.99 eV in Figure 4c), $E_{a,eff}^{diff}$ dominates over $E_{a,eff}^{det}$ for most low-energy pairs, making diffusion the activity-limiting step. Whether Au or AuO diffusion controls a pair depends on the FS energy difference, as the intrinsic diffusion barriers of the two species already differ. Consequently, the overall barrier is insensitive to E_a^{det}. A 1-2 eV variation yields negligible changes (Figure S29) unless E_a^{det} is sufficiently large (e.g. 2 eV) to satisfy $E_{IS}+E_a^{det} > E_{FS}+E_a^{diff}$, where detachment becomes rate-limiting.

The overall mechanism for the OR of Au_nO_m nanocluster on $TiO_2(101)$ is summarized in Figure 5. The kinetically preferred route is the one minimizing $\max(E_{a,eff,i}^{det}, E_{a,eff,i}^{diff})$ over all IS-FS pairs, and it proceeds in three stages:

1. Detachment. A AuO_x monomer is released from the Au_nO_m cluster via a specific IS configuration, with E_a^{det} ranging from 1 to 2 eV depending on the IS structure and the local environment of the detaching

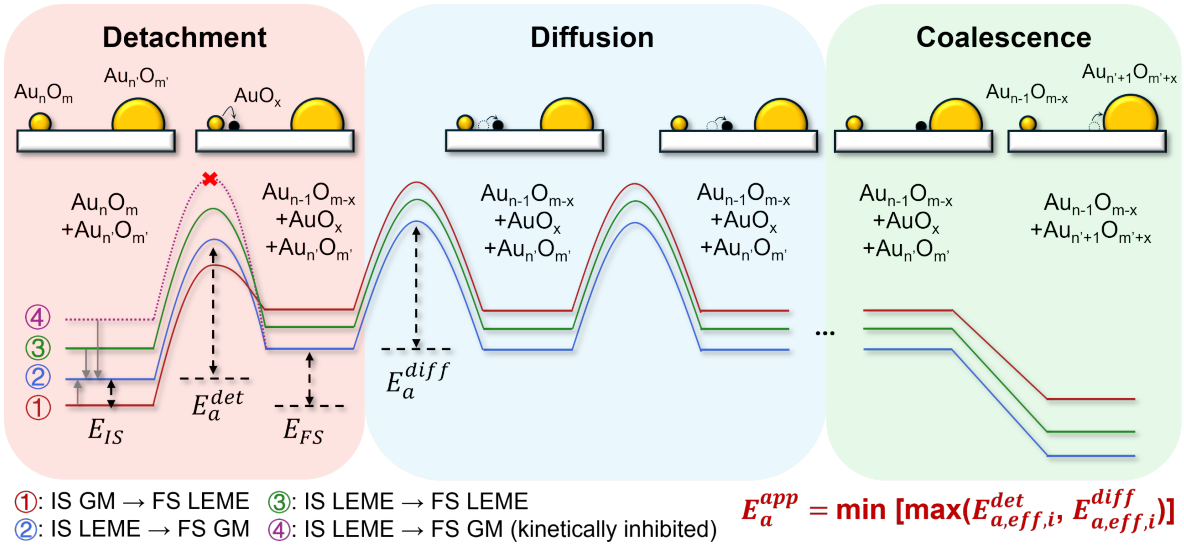

Figure 5. Overall mechanism for the OR of Au_nO_m nanocluster on the TiO_2(101) surface.

monomer. The step is endothermic, and the energy of the resulting FS depends strongly on the IS from which detachment occurs.

2. Diffusion. The detached monomer migrates away from the parent cluster with a constant intrinsic barrier E_a^{diff} (0.19 and 0.74 eV for Au on O-free and O-adsorbed clusters, 0.99 eV for AuO). This step is thermoneutral once the monomer is sufficiently separated from the cluster.
3. Coalescence. The monomer merges with a larger $Au_{n'}O_{m'}$ cluster, making the overall ripening process exothermic.

Because detachment is strongly endothermic, OR is predominantly diffusion-controlled, and the overall barrier is governed by E_{FS}. The system therefore favors reaching the lowest-energy FS. Since isomerization is faster than detachment, a general IS LEME configuration first isomerizes to the optimal IS LEME configuration and then detaches to the FS GM (Pathway ③→②), rather than detaching from the IS GM, which can only reach a higher-energy FS LEME structure (Pathway ①). A low FS alone is not sufficient, however, an IS LEME structure reaching the FS GM but with too high a detachment barrier is bypassed (Pathway ④, dotted line) in favor of an alternative low-barrier IS. Detachment becomes rate-limiting only when $E_{IS}+E_a^{det} > E_{FS}+E_a^{diff}$.

4. Discussion on the Cluster-Size- and O-Coverage-Dependent Ostwald Ripening

We applied a kinetic model to determine E_a^{app} for the OR process of $Au_{12}O_3$, accounting for the effective detachment and diffusion barriers of Au and AuO (Eq. 5 and Eq. 6). This model relates E_a^{app} to E_{IS}, E_{FS}, E_a^{det} and E_a^{diff} for each IS-FS pair identified by MDMAP. We the extended it to evaluate the OR kinetics of Au_nO_m nanoclusters on TiO_2(101) across three sizes (n=12, 30, 50) and various oxygen contents to study the effect of cluster size and O coverage. For each size, the oxygen content spanned from zero to saturation under ambient conditions (298 K, 0.21 bar O_2). Specifically, when m=0, AuO detachment entails the removal of an O_{2c} atom from the TiO_2(101) surface. MDMAP was applied to 17 Au_nO_m/TiO_2(101) systems, utilizing the configurations identified by global optimization in our previous work[54]. E_{IS} and E_{FS} were verified by single-point DFT calculations on selected structures (details in SI Section 6.3). As in Section 3.3, we used E_a^{det} = 1.38 and 1.46 eV for Au and AuO detachment, and E_a^{diff} = 0.19 eV (Au, O-free clusters), 0.74 eV (Au, O-adsorbed clusters), and 0.99 eV (AuO).

Figure 6a illustrates E_a^{app} (triangles) and E_{IS} (squares) of the globally optimal OR pathway for Au_nO_m nanoclusters on TiO_2(101) across compositions. The x-axis is the ratio of adsorbed oxygen atoms to surface Au atoms (O_{ad}/Au_{surf}, see SI Section 1.2 for the identification of surface Au). Further details, including the IS-FS maps of the OR overall barrier, are provided in Table S5 and Figure S31-S33. The E_{IS} indicate that most OR pathways proceed through an IS LEME (E_{IS}=0.03~0.63 eV) rather than the IS GM. For comparison, the E_a^{app} value obtained when only the IS GM pathway is considered is also shown (purple dotted line). Neglecting the LEME in this way underestimates the barrier by up to 0.67 eV. These results demonstrate the importance of the LEME structures in accounting for OR kinetics.

Beyond the role of the LEME, the presence of O_{ad} itself strongly affects the kinetics. For the larger clusters (Au_{30} and Au_{50}), introducing O_{ad} generally lowers E_a^{app} to below 2.2 eV, compared with above 2.6 eV for the O_{ad}-free clusters. In the absence of O_{ad} (O_{ad}/Au_{surf}=0), E_a^{app} follows the order of $Au_{12} < Au_{50} < Au_{30}$, suggesting that the kinetic shrinking of Au_{50} is faster than that of Au_{30}. However, this does not imply a conversion from Au_{50} to Au_{30}, as larger clusters are inherently more thermodynamically stable. To elucidate the promotional role of these O_{ad} atoms, we analyzed the net Bader charge (Figure 6b and Figure S34). For an ideal detachment process, the

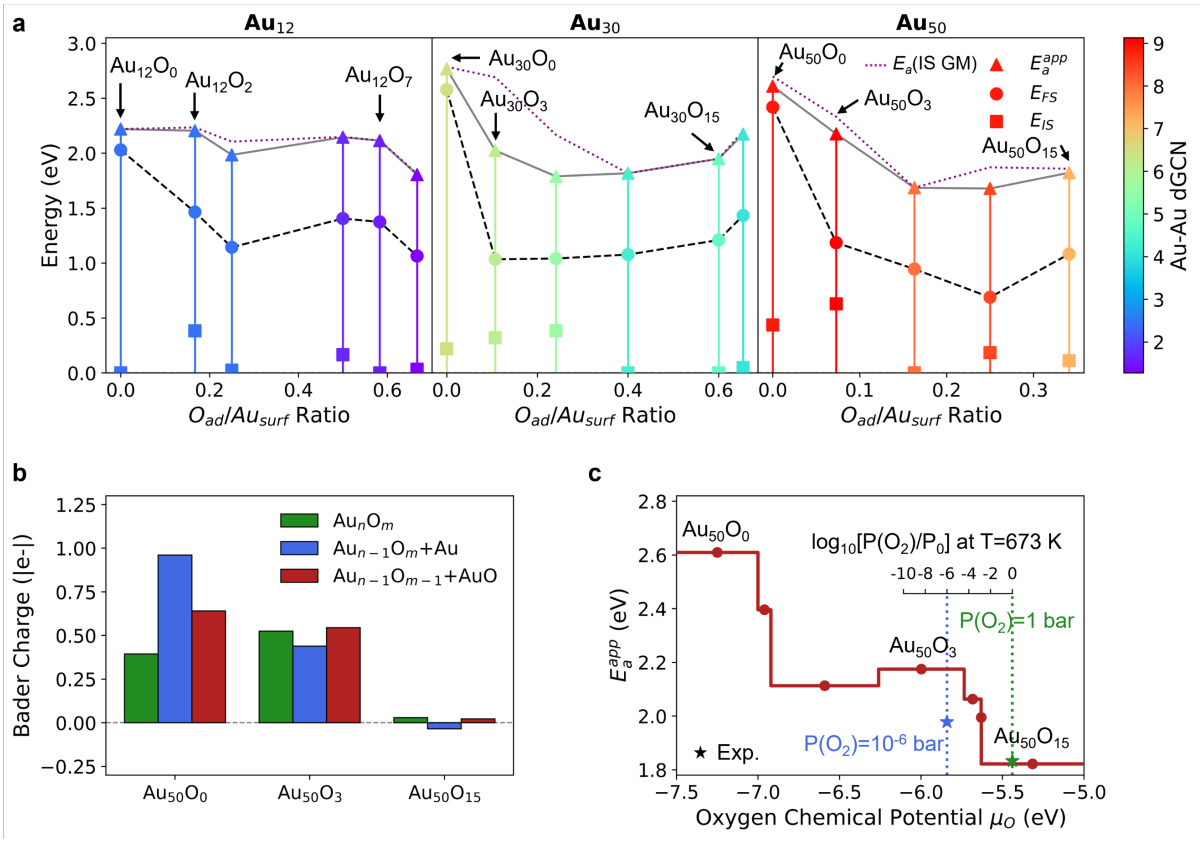

Figure 6. (a) Calculated apparent activation energy (E_a^{app}) for the OR of Au_nO_m nanoclusters at three sizes (n=12, 30 and 50) with various O contents on the TiO_2(101) surface. The detachment IS and FS energies for each O content are denoted by squares and circles, respectively. The color scale represents the Boltzmann-weighted Au-Au dGCN for the nanocluster ensemble. The black dashed line indicates the detachment reaction energy, while the purple dotted line represents the E_a^{app} when considering only the pathway via the IS GM. (b) Net Bader charge of the $Au_{50}O_m$ nanocluster before detachment (Au_nO_m, green), and the coexisting parent cluster and monomer after detachment ($Au_{n-1}O_m$+Au, blue and $Au_{n-1}O_{m-1}$+AuO, red). (c) E_a^{app} for $Au_{50}O_m$ at 673 K. The stars denote the E_a^{app} values evaluated from the experiment[28].

total charge after detachment (cluster + monomer) should equal the initial cluster charge, meaning no electron transfer occurs between the Au species and the TiO_2 substrate. During Au detachment, without O_{ad}, the total charge changes from +0.39 |e| ($Au_{50}O_0$) to +0.96 |e| (Au_{49}+Au). This loss of electrons to the TiO_2 substrate creates a high energy penalty and destabilizes the interface. With O_{ad}, however, the total charge before and after detachment is almost identical (+0.53 vs +0.44 |e| for $Au_{50}O_3$ and +0.03 vs -0.04 |e| for $Au_{50}O_{15}$). O_{ad} provides low-energy vacant states to maintain this local charge balance[54,76], successfully lowering E_a^{app}. For AuO detachment, the same rule applies. Without O_{ad}, the total charge after detachment (+0.64 |e|) deviates significantly from the initial value (+0.39 |e|), leading to instability. In contrast, the presence of O_{ad} maintains a stable total charge throughout the detachment process, preserving interfacial stability. The modulation of charge levels by O adsorption and its subsequent impact on the reaction energetics have also been previously discussed by Wang et al.[39]

Figure 6a further indicates that the trend of the E_a^{app} with varying oxygen content is strongly correlated with the cluster size and the Au-Au dGCN. For larger nanoclusters (Au_{30} and Au_{50}), E_a^{app} decreases first and then increases slightly as the oxygen content rises. The black dashed line guides the detachment reaction energy E_{FS} of the optimal pathway, whose trend closely matches that of E_a^{app}. Both E_{FS} and E_a^{app} are controlled by the Au-Au dGCN: more oxygen lowers the Au-Au dGCN, which makes detachment easier and lowers E_{FS}. Since E_{FS} also enters the effective diffusion barrier (Eq. 6), a lower E_{FS} lowers E_a^{app} as well. This trend is robust to the value of E_a^{det}.

The trend follows how oxygen reshapes the cluster. At low oxygen content (O_{ad}/Au_{surf}=0~0.1), the gold cores are highly close-packed with high Au-Au dGCN values (6.1 for $Au_{30}O_3$ and 9.1 for $Au_{50}O_3$). This close-packed structure (See Figure S43 and S45) makes monomer detachment unfavorable, leading to a large E_{FS} (1.03/1.18 eV) and higher E_a^{app} (2.02/2.17 eV). At moderate coverage (O_{ad}/Au_{surf}=0.15~0.60), the cluster structure becomes less ordered and less close-packed (Au-Au dGCN drops to 4.8-5.6 for Au_{30} and 7.1-8.4 for Au_{50}), making detachment easier and lowering E_a^{app} (1.79-1.95 eV/1.68-1.82 eV). Too much O_{ad} forms a gold-oxide-like network that stabilizes the structure, raising E_a^{app} again (e.g., 2.17 eV for $Au_{30}O_{17}$ at high O_{ad}/Au_{surf}=0.65). In contrast, for the small Au_{12} cluster, its size intrinsically prevents a close-packed structure, maintaining a low Au-Au dGCN (1.2~2.4) and E_a^{app} (2.0-2.2 eV) regardless of oxygen content. Overall, our findings demonstrate that moderate oxygen coverage on large clusters (Au_{30} and Au_{50}) promotes sintering kinetics by stabilizing the charge transfer between the monomer and cluster and lowering the Au-Au dGCN, which effectively reduces the E_a^{app}.

Furthermore, we calculated E_a^{app} of OR for the $Au_{50}O_m$ nanoclusters (up to 1.5 nm) at 673 K over a wide range of oxygen chemical potential μ_O, spanning from -7.5 to -5.0 eV (See Figure S47 for the $Au_{50}O_m$ thermodynamics). Figure 6c illustrates the variation of E_a^{app} as a function of μ_O, showing seven stable compositions: $Au_{50}O_0$, $Au_{50}O_1$, $Au_{50}O_2$, $Au_{50}O_3$, $Au_{50}O_4$, $Au_{50}O_5$ and $Au_{50}O_{15}$. The typical experimental window corresponds to μ_O between -6.2 and -5.4 eV ($P(O_2)$ from 10^{-10} to 1 bar at 673 K) as indicated in Figure 6c. Within this experimentally relevant regime, $Au_{50}O_3$, $Au_{50}O_4$, $Au_{50}O_5$ and $Au_{50}O_{15}$ emerge as the thermodynamically stable phases. Our calculations show that E_a^{app} drops from 2.17 to 1.82 eV as μ_O increases from -6.2 eV to -5.4 eV, indicating that the OR process of Au_{50} is significantly promoted under more oxidizing conditions.

This theoretical trend aligns well with experimental observations of oxygen-induced sintering in Au nanoparticles (~3 nm). For instance, TEM studies by Li et al.[28] examined the evolution of Au particle sizes under different gas atmospheres (1 bar Ar, CO, O_2 and mixed CO+O_2), and found that oxygen-rich environments facilitate sintering via both PMC and OR. Specifically, on the TiO_2(101) surface at 673 K, the Au particles grew from 3.1 to 10.3 nm within 48 h under 1 bar O_2 (μ_O=-5.45 eV, green dashed line in Figure 6c), whereas they grew to only 4.9 nm under 1 bar Ar (containing 1 ppm O_2 impurity, μ_O=-5.85 eV, blue dashed line in Figure 6c). The sintering barriers that we evaluated from their experimental kinetics (See SI Section 6.10) are 1.98 eV for μ_O=-5.45 eV and 1.83 eV for μ_O=-5.85 eV (stars in Figure 6c), which is consistent with our theoretical results. Similarly, Masoud et al[77] reported that the growth of Au nanoparticles (from 3 to 8 nm) on rutile TiO_2 is

significantly accelerated under oxidizing atmospheres at 773 K. Beyond the comparison of apparent barriers made here, the full detachment and diffusion energetics could serve as input for kinetic Monte Carlo simulations of nucleation and growth, enabling direct comparison with time-resolved kinetic experiments.

Notably, the suppressed effect under excessive oxidation predicted for our sub-1.5 nm clusters (e.g. $Au_{30}O_{17}$) is rarely observed experimentally. This discrepancy likely stems from a size effect: smaller clusters are highly sensitive to oxygen coverage due to their high surface-to-volume ratio and low atomic coordination, leading to over-oxidation that suppresses mobility. In contrast, larger experimental particles (≥ 3 nm) possess a more robust metallic core and a lower proportion of interfacial sites, making them less susceptible to over-oxidation and allowing oxygen-induced sintering to prevail.

Our results suggest that OR affects catalytic performance not only through particle coarsening, which reduces the fraction of low-coordinated active sites, but also through the evolution of the Au/TiO_2 interface. Changes in interfacial oxygen species and cluster-support charge transfer may modify reactant adsorption and activation, thereby influencing catalytic activity.

5. Conclusion

We systematically investigated the OR mechanism for Au nanoclusters on the anatase TiO_2(101) surface using a Au-Ti-O neural network potential. Global optimization identified the Au adatom and AuO monomer as the predominant mobile species under oxidizing conditions. Both species adopt a characteristic [O-Au-O] coordination motif: the Au adatom bridges two surface O_{2c} atoms ($Au_{O2c\text{-}b}$), while the AuO monomer bonds with a surface O_{1c} atom generated via the cleavage of a Ti-O_{2c} bond ($Au_{O1c}O$).

By implementing a systematic MDMAP workflow, we mapped the energetic landscape of monomer detachment for supported Au_nO_m clusters. MDMAP provides the ensemble of candidate IS and FS structures for studying the OR mechanism, on which the detachment and diffusion barriers are then evaluated. Intrinsic detachment barriers (E_a^{det}) range from 1 to 2 eV depending on the IS structure and the local environment of the detaching monomer, whereas monomer diffusion has a much lower and nearly constant intrinsic barrier (E_a^{diff}=0.19 eV for Au with O-free cluster, 0.74 eV for Au with O-adsorbed cluster and 0.99 eV for AuO). Since detachment and diffusion occur in series, the overall barrier of a pathway is the higher of the two, and OR follows the IS-FS pair minimizing this value. The apparent activation energy is thus $E_a^{app} = \min[\max(E_{a,eff,i}^{det}, E_{a,eff,i}^{diff})]$. This analysis shows that the optimal pathway proceeds through low-energy metastable (LEME) rather than ground-state (GM) configurations. Neglecting the LEME underestimates E_a^{app} by up to 0.67 eV.

By evaluating clusters of various sizes and oxygen contents, we further elucidated the key role of interfacial oxygen in governing OR kinetics. A key methodological and physical insight of our work is that OR cannot be accurately described by treating the detaching monomer as an isolated species. Instead, the nanocluster acts as an essential electronic reservoir, participating in a charge-transfer interaction. Moderate oxygen coverage significantly accelerates sintering kinetics by maintaining local interfacial charge balance and lowering Au-Au coordination numbers, which reduces the apparent activation energy. Conversely, excessive oxidation stabilizes these sub-nanometer clusters against monomer loss.

These insights provide a robust theoretical foundation for the rational design of sintering-resistant catalysts. By precisely tuning the interfacial environment, specifically the oxygen coverage, it is possible to balance catalytic activity with long-term stability. Furthermore, our generalizable methodology bridges atomistic electronic structures with macroscopic kinetics, offering a powerful framework to explore complex ripening mechanisms in diverse supported metal systems and optimize catalytic longevity under reactive atmospheres.

Associated Content

Supporting Information Supplementary methods, model of Au/TiO_2(101), configurations and electronic states

of AuO_x monomers, MDMAP of $Au_{12}O_3/TiO_2(101)$, pathways of Au and AuO detachment and diffusion, Au_nO_m Ostwald ripening kinetics.
XYZ Coordinates of AuO_x monomers and detachment ISs and FSs for the optimal OR pathways.
Training dataset for Au−Ti−O NN potential used in this work is publicly available on Zenodo.
Preliminary URL (will be updated upon publication):
https://zenodo.org/records/19140458?preview=1&token=eyJhbGciOiJIUzUxMiJ9.eyJpZCI6ImU3ZDQ1N2UzLTljNjAtNDE2Ni04YzM1LTI3ZjIxNjg1MmZiMSIsImRhdGEiOnt9LCJyYW5kb20iOiI1MGI3ZmY4NTczZGJkMTk0NDU0YTM5NWM2YzgwNmFjZSJ9.mccV-GUj_dTphC32sIXhg7df5rzEJNvrP8zIJgFGjVOEEYIuZd_3FlMKK8YwHmkpQyTdLomMgpMeU4bTvrtkVQ

Author Information

Corresponding Author
Philippe Sautet - Department of Chemical and Biomolecular Engineering, University of California, Los Angeles, California 90095, United States
Email: sautet@ucla.edu
Authors
Qian-Yu Liu - Department of Chemistry and Biochemistry, University of California, Los Angeles, California 90095, United States
Dongxiao Chen - Department of Chemistry and Biochemistry, University of California, Los Angeles, California 90095, United States
Notes
The authors declare no competing financial interest.

Acknowledgments

This work was supported by the U.S. Defense Threat Reduction Agency under Award Number HDTR1211001612 and the Audi CO_2 CyPres Award. DC and PS were supported by the National Science Foundation CDS&E grant 2152767. Computations in this work were performed on the Hoffman2 cluster at UCLA Institute for Digital Research and Education (IDRE), and the Bridges2 cluster through allocation CHE170060 from the Advanced Cyberinfrastructure Coordination Ecosystem: Services & Support (ACCESS) supported by the National Science Foundation.

References

(1) Liu, L.; Corma, A. Metal Catalysts for Heterogeneous Catalysis: From Single Atoms to Nanoclusters and Nanoparticles. *Chem. Rev.* **2018**, *118* (10), 4981–5079. https://doi.org/10.1021/acs.chemrev.7b00776.
(2) Munnik, P.; de Jongh, P. E.; de Jong, K. P. Recent Developments in the Synthesis of Supported Catalysts. *Chem. Rev.* **2015**, *115* (14), 6687–6718. https://doi.org/10.1021/cr500486u.
(3) Parastaev, A.; Muravev, V.; Huertas Osta, E.; van Hoof, A. J. F.; Kimpel, T. F.; Kosinov, N.; Hensen, E. J. M. Boosting CO_2 Hydrogenation via Size-Dependent Metal–Support Interactions in Cobalt/Ceria-Based Catalysts. *Nat. Catal.* **2020**, *3* (6), 526–533. https://doi.org/10.1038/s41929-020-0459-4.
(4) Sankar, M.; He, Q.; Engel, R. V.; Sainna, M. A.; Logsdail, A. J.; Roldan, A.; Willock, D. J.; Agarwal, N.; Kiely, C. J.; Hutchings, G. J. Role of the Support in Gold-Containing Nanoparticles as Heterogeneous Catalysts. *Chem. Rev.* **2020**, *120* (8), 3890–3938. https://doi.org/10.1021/acs.chemrev.9b00662.
(5) Wang, T.; Hu, J.; Ouyang, R.; Wang, Y.; Huang, Y.; Hu, S.; Li, W.-X. Nature of Metal-Support Interaction for Metal Catalysts on Oxide Supports. *Science* **2024**, *386* (6724), 915–920. https://doi.org/10.1126/science.adp6034.
(6) Jiang, C.; Yan, B.; Goldsmith, B. R.; Linic, S. Predictive Model for the Discovery of Sinter-Resistant Supports for Metallic Nanoparticle Catalysts by Interpretable Machine Learning. *Nat. Catal.* **2025**, *8* (10), 1038–1050. https://doi.org/10.1038/s41929-025-01417-3.
(7) Haruta, M. Size- and Support-Dependency in the Catalysis of Gold. *Catal. Today* **1997**, *36* (1), 153–166. https://doi.org/10.1016/S0920-5861(96)00208-8.

(8) Valden, M.; Lai, X.; Goodman, D. W. Onset of Catalytic Activity of Gold Clusters on Titania with the Appearance of Nonmetallic Properties. *Science* **1998**, *281* (5383), 1647–1650. https://doi.org/10.1126/science.281.5383.1647.
(9) Emmanuel, J.; Hayden, B. E.; Saleh-Subaie, J. The Particle Size Dependence of CO Oxidation on Model Planar Titania Supported Gold Catalysts Measured by Parallel Thermographic Imaging. *J. Catal.* **2019**, *369*, 175–180. https://doi.org/10.1016/j.jcat.2018.10.038.
(10) Ishida, T.; Murayama, T.; Taketoshi, A.; Haruta, M. Importance of Size and Contact Structure of Gold Nanoparticles for the Genesis of Unique Catalytic Processes. *Chem. Rev.* **2020**, *120* (2), 464–525. https://doi.org/10.1021/acs.chemrev.9b00551.
(11) Campbell, C. T.; Parker, S. C.; Starr, D. E. The Effect of Size-Dependent Nanoparticle Energetics on Catalyst Sintering. *Science* **2002**, *298* (5594), 811–814. https://doi.org/10.1126/science.1075094.
(12) Hansen, T. W.; DeLaRiva, A. T.; Challa, S. R.; Datye, A. K. Sintering of Catalytic Nanoparticles: Particle Migration or Ostwald Ripening? *Acc. Chem. Res.* **2013**, *46* (8), 1720–1730. https://doi.org/10.1021/ar3002427.
(13) Hu, S.; Li, W.-X. Sabatier Principle of Metal-Support Interaction for Design of Ultrastable Metal Nanocatalysts. *Science* **2021**, *374* (6573), 1360–1365. https://doi.org/10.1126/science.abi9828.
(14) Haruta, M.; Kobayashi, T.; Sano, H.; Yamada, N. Novel Gold Catalysts for the Oxidation of Carbon Monoxide at a Temperature Far Below 0 °C. *Chem. Lett.* **1987**, *16* (2), 405–408. https://doi.org/10.1246/cl.1987.405.
(15) Liu, Z.-P. Catalytic Role of Metal Oxides in Gold-Based Catalysts: A First Principles Study of CO Oxidation on TiO2 Supported Au. *Phys. Rev. Lett.* **2003**, *91* (26), 266102. https://doi.org/10.1103/PhysRevLett.91.266102.
(16) Wang, Y.-G.; Yoon, Y.; Glezakou, V.-A.; Li, J.; Rousseau, R. The Role of Reducible Oxide–Metal Cluster Charge Transfer in Catalytic Processes: New Insights on the Catalytic Mechanism of CO Oxidation on Au/TiO_2 from Ab Initio Molecular Dynamics. *J. Am. Chem. Soc.* **2013**, *135* (29), 10673–10683. https://doi.org/10.1021/ja402063v.
(17) Green, I. X.; Tang, W.; Neurock, M.; Yates, J. T. Jr. Insights into Catalytic Oxidation at the Au/TiO2 Dual Perimeter Sites. *Acc. Chem. Res.* **2014**, *47* (3), 805–815. https://doi.org/10.1021/ar400196f.
(18) Duan, Z.; Henkelman, G. CO Oxidation at the Au/TiO_2 Boundary: The Role of the Au/Ti_{5c} Site. *ACS Catal.* **2015**, *5* (3), 1589–1595. https://doi.org/10.1021/cs501610a.
(19) Yuan, W.; Zhu, B.; Fang, K.; Li, X.-Y.; Hansen, T. W.; Ou, Y.; Yang, H.; Wagner, J. B.; Gao, Y.; Wang, Y.; Zhang, Z. In Situ Manipulation of the Active Au-TiO2 Interface with Atomic Precision during CO Oxidation. *Science* **2021**, *371* (6528), 517–521. https://doi.org/10.1126/science.abe3558.
(20) Hayashi, T.; Tanaka, K.; Haruta, M. Selective Vapor-Phase Epoxidation of Propylene over Au/TiO_2 Catalysts in the Presence of Oxygen and Hydrogen. *J. Catal.* **1998**, *178* (2), 566–575. https://doi.org/10.1006/jcat.1998.2157.
(21) Qi, C.; Akita, T.; Okumura, M.; Haruta, M. Epoxidation of Propylene over Gold Catalysts Supported on Non-Porous Silica. *Appl. Catal. Gen.* **2001**, *218* (1), 81–89. https://doi.org/10.1016/S0926-860X(01)00621-4.
(22) Lee, S.; Molina, L. M.; López, M. J.; Alonso, J. A.; Hammer, B.; Lee, B.; Seifert, S.; Winans, R. E.; Elam, J. W.; Pellin, M. J.; Vajda, S. Selective Propene Epoxidation on Immobilized Au6–10 Clusters: The Effect of Hydrogen and Water on Activity and Selectivity. *Angew. Chem. Int. Ed.* **2009**, *48* (8), 1467–1471. https://doi.org/10.1002/anie.200804154.
(23) Kanungo, S.; Su, Y.; d'Angelo, M. F. N.; Schouten, J. C.; Hensen, E. J. M. Epoxidation of Propene Using Au/TiO_2: On the Difference between H_2 and CO as a Co-Reactant. *Catal. Sci. Technol.* **2017**, *7* (11), 2252–2261. https://doi.org/10.1039/C7CY00525C.
(24) Tsukamoto, D.; Shiraishi, Y.; Sugano, Y.; Ichikawa, S.; Tanaka, S.; Hirai, T. Gold Nanoparticles Located at the Interface of Anatase/Rutile TiO_2 Particles as Active Plasmonic Photocatalysts for Aerobic Oxidation. *J. Am. Chem. Soc.* **2012**, *134* (14), 6309–6315. https://doi.org/10.1021/ja2120647.
(25) Chen, Y.; Soler, L.; Cazorla, C.; Oliveras, J.; Bastús, N. G.; Puntes, V. F.; Llorca, J. Facet-Engineered TiO_2 Drives Photocatalytic Activity and Stability of Supported Noble Metal Clusters during H_2 Evolution. *Nat. Commun.* **2023**, *14* (1), 6165. https://doi.org/10.1038/s41467-023-41976-2.

(26) Kao, K.-C.; Huang, S.-J.; Hsia, Y.-F.; Huang, J.-H.; Mou, C.-Y. Supported Au Nanoparticles on TiO_2 for Visible Light Photocatalytic H_2O_2 Production: Effects of Au Particle Size and Density. *ACS Appl. Nano Mater.* **2024**, *7* (1), 218–229. https://doi.org/10.1021/acsanm.3c04340.
(27) Yuan, W.; Zhang, D.; Ou, Y.; Fang, K.; Zhu, B.; Yang, H.; Hansen, T. W.; Wagner, J. B.; Zhang, Z.; Gao, Y.; Wang, Y. Direct In Situ TEM Visualization and Insight into the Facet-Dependent Sintering Behaviors of Gold on TiO_2. *Angew. Chem. Int. Ed.* **2018**, *57* (51), 16827–16831. https://doi.org/10.1002/anie.201811933.
(28) Li, G.; Fang, K.; Chen, Y.; Ou, Y.; Mao, S.; Yuan, W.; Wang, Y.; Yang, H.; Zhang, Z.; Wang, Y. Unveiling the Gas-Dependent Sintering Behavior of Au-TiO_2 Catalysts via Environmental Transmission Electron Microscopy. *J. Catal.* **2020**, *388*, 84–90. https://doi.org/10.1016/j.jcat.2020.05.003.
(29) Yang, F.; Chen, M. S.; Goodman, D. W. Sintering of Au Particles Supported on TiO_2(110) during CO Oxidation. *J. Phys. Chem. C* **2009**, *113* (1), 254–260. https://doi.org/10.1021/jp807865w.
(30) Simonsen, S. B.; Chorkendorff, I.; Dahl, S.; Skoglundh, M.; Sehested, J.; Helveg, S. Direct Observations of Oxygen-Induced Platinum Nanoparticle Ripening Studied by In Situ TEM. *J. Am. Chem. Soc.* **2010**, *132* (23), 7968–7975. https://doi.org/10.1021/ja910094r.
(31) Suzuki, A.; Inada, Y.; Yamaguchi, A.; Chihara, T.; Yuasa, M.; Nomura, M.; Iwasawa, Y. Time Scale and Elementary Steps of CO-Induced Disintegration of Surface Rhodium Clusters. *Angew. Chem. Int. Ed.* **2003**, *42* (39), 4795–4799. https://doi.org/10.1002/anie.200352318.
(32) Liu, J.-C.; Luo, L.; Xiao, H.; Zhu, J.; He, Y.; Li, J. Metal Affinity of Support Dictates Sintering of Gold Catalysts. *J. Am. Chem. Soc.* **2022**, *144* (45), 20601–20609. https://doi.org/10.1021/jacs.2c06785.
(33) Xu, J.; Das, S.; Pathak, A. D.; Patra, A.; Shetty, S.; Hohl, D.; Car, R. Dynamic Metal–Support Interaction Dictates Cu Nanoparticle Sintering on Al_2O_3 Surfaces. *ACS Nano* **2025**, *19* (32), 29242–29254. https://doi.org/10.1021/acsnano.5c04622.
(34) Alghannam, A.; Muhich, C. L.; Musgrave, C. B. Adatom Surface Diffusion of Catalytic Metals on the Anatase TiO_2(101) Surface. *Phys. Chem. Chem. Phys.* **2017**, *19* (6), 4541–4552. https://doi.org/10.1039/C6CP08789B.
(35) Ouyang, R.; Liu, J.-X.; Li, W.-X. Atomistic Theory of Ostwald Ripening and Disintegration of Supported Metal Particles under Reaction Conditions. *J. Am. Chem. Soc.* **2013**, *135* (5), 1760–1771. https://doi.org/10.1021/ja3087054.
(36) Parkinson, G. S.; Novotny, Z.; Argentero, G.; Schmid, M.; Pavelec, J.; Kosak, R.; Blaha, P.; Diebold, U. Carbon Monoxide-Induced Adatom Sintering in a Pd–Fe_3O_4 Model Catalyst. *Nat. Mater.* **2013**, *12* (8), 724–728. https://doi.org/10.1038/nmat3667.
(37) Liu, J.-C.; Wang, Y.-G.; Li, J. Toward Rational Design of Oxide-Supported Single-Atom Catalysts: Atomic Dispersion of Gold on Ceria. *J. Am. Chem. Soc.* **2017**, *139* (17), 6190–6199. https://doi.org/10.1021/jacs.7b01602.
(38) Zhang, S.; Han, Y.; Li, X.-Y.; Tang, Q.; Zhu, B.; Gao, Y. Particle Hopping and Coalescence of Supported Au Nanoparticles in Harsh Reactive Environments. *J. Am. Chem. Soc.* **2025**, *147* (18), 15796–15805. https://doi.org/10.1021/jacs.5c03633.
(39) Wang, Y.-G.; Cantu, D. C.; Lee, M.-S.; Li, J.; Glezakou, V.-A.; Rousseau, R. CO Oxidation on Au/TiO_2: Condition-Dependent Active Sites and Mechanistic Pathways. *J. Am. Chem. Soc.* **2016**, *138* (33), 10467–10476. https://doi.org/10.1021/jacs.6b04187.
(40) Zhai, H.; Alexandrova, A. N. Ensemble-Average Representation of Pt Clusters in Conditions of Catalysis Accessed through GPU Accelerated Deep Neural Network Fitting Global Optimization. *J. Chem. Theory Comput.* **2016**, *12* (12), 6213–6226. https://doi.org/10.1021/acs.jctc.6b00994.
(41) Zhai, H.; Alexandrova, A. N. Fluxionality of Catalytic Clusters: When It Matters and How to Address It. *ACS Catal.* **2017**, *7* (3), 1905–1911. https://doi.org/10.1021/acscatal.6b03243.
(42) Zhang, Z.; Zandkarimi, B.; Alexandrova, A. N. Ensembles of Metastable States Govern Heterogeneous Catalysis on Dynamic Interfaces. *Acc. Chem. Res.* **2020**, *53* (2), 447–458. https://doi.org/10.1021/acs.accounts.9b00531.
(43) Sun, G.; Sautet, P. Active Site Fluxional Restructuring as a New Paradigm in Triggering Reaction Activity for Nanocluster Catalysis. *Acc. Chem. Res.* **2021**, *54* (20), 3841–3849. https://doi.org/10.1021/acs.accounts.1c00413.

(44) Sun, J.-J.; Cheng, J. Solid-to-Liquid Phase Transitions of Sub-Nanometer Clusters Enhance Chemical Transformation. *Nat. Commun.* **2019**, *10* (1), 5400. https://doi.org/10.1038/s41467-019-13509-3.
(45) Zandkarimi, B.; Poths, P.; Alexandrova, A. N. When Fluxionality Beats Size Selection: Acceleration of Ostwald Ripening of Sub-Nano Clusters. *Angew. Chem. Int. Ed.* **2021**, *60* (21), 11973–11982. https://doi.org/10.1002/anie.202100107.
(46) Poths, P.; Hong, Z.; Li, G.; Anderson, S. L.; Alexandrova, A. N. "Magic" Sinter-Resistant Cluster Sizes of Pt_n Supported on Alumina. *J. Phys. Chem. Lett.* **2022**, *13* (47), 11044–11050. https://doi.org/10.1021/acs.jpclett.2c03114.
(47) Chen, D.; Sautet, P. Atomistic Landscape of Pt Nanoparticles via Machine Learning: How Size Effect and Hydrogen Adsorption Govern Structural Ensembles and Catalytic Activity. *Angew. Chem. Int. Ed.* **2026**, *65* (2), e19209. https://doi.org/10.1002/anie.202519209.
(48) Shang, C.; Liu, Z.-P. Stochastic Surface Walking Method for Structure Prediction and Pathway Searching. *J. Chem. Theory Comput.* **2013**, *9* (3), 1838–1845. https://doi.org/10.1021/ct301010b.
(49) Shang, C.; Zhang, X.-J.; Liu, Z.-P. Stochastic Surface Walking Method for Crystal Structure and Phase Transition Pathway Prediction. *Phys. Chem. Chem. Phys.* **2014**, *16* (33), 17845–17856. https://doi.org/10.1039/C4CP01485E.
(50) Sun, G.; Fuller, J. T. I.; Alexandrova, A. N.; Sautet, P. Global Activity Search Uncovers Reaction Induced Concomitant Catalyst Restructuring for Alkane Dissociation on Model Pt Catalysts. *ACS Catal.* **2021**, *11* (3), 1877–1885. https://doi.org/10.1021/acscatal.0c05421.
(51) Liu, Q.-Y.; Chen, D.; Shang, C.; Liu, Z.-P. An Optimal Fe–C Coordination Ensemble for Hydrocarbon Chain Growth: A Full Fischer–Tropsch Synthesis Mechanism from Machine Learning. *Chem. Sci.* **2023**, *14* (35), 9461–9475. https://doi.org/10.1039/D3SC02054A.
(52) Kang, P.-L.; Yang, Z.-X.; Shang, C.; Liu, Z.-P. Global Neural Network Potential with Explicit Many-Body Functions for Improved Descriptions of Complex Potential Energy Surface. *J. Chem. Theory Comput.* **2023**, *19* (21), 7972–7981. https://doi.org/10.1021/acs.jctc.3c00873.
(53) Huang, S.-D.; Shang, C.; Kang, P.-L.; Zhang, X.-J.; Liu, Z.-P. LASP: Fast Global Potential Energy Surface Exploration. *WIREs Comput. Mol. Sci.* **2019**, *9* (6), e1415. https://doi.org/10.1002/wcms.1415.
(54) Liu, Q.-Y.; Li, Y.; Chen, D.; Sautet, P. Size- and Facet-Dependent Behavior of Electron Storage at the Au/Anatase TiO_2 Interface under Ambient Conditions from Machine Learning. *ACS Catal.* **2025**, *15* (22), 19057–19069. https://doi.org/10.1021/acscatal.5c05415.
(55) Zhang, X.-J.; Shang, C.; Liu, Z.-P. Double-Ended Surface Walking Method for Pathway Building and Transition State Location of Complex Reactions. *J. Chem. Theory Comput.* **2013**, *9* (12), 5745–5753. https://doi.org/10.1021/ct4008475.
(56) Zhang, X.-J.; Liu, Z.-P. Variable-Cell Double-Ended Surface Walking Method for Fast Transition State Location of Solid Phase Transitions. *J. Chem. Theory Comput.* **2015**, *11* (10), 4885–4894. https://doi.org/10.1021/acs.jctc.5b00641.
(57) Huang, S.-D.; Shang, C.; Kang, P.-L.; Liu, Z.-P. Atomic Structure of Boron Resolved Using Machine Learning and Global Sampling. *Chem. Sci.* **2018**, *9* (46), 8644–8655. https://doi.org/10.1039/C8SC03427C.
(58) Behler, J. Representing Potential Energy Surfaces by High-Dimensional Neural Network Potentials. *J. Phys. Condens. Matter* **2014**, *26* (18), 183001. https://doi.org/10.1088/0953-8984/26/18/183001.
(59) Behler, J.; Parrinello, M. Generalized Neural-Network Representation of High-Dimensional Potential-Energy Surfaces. *Phys. Rev. Lett.* **2007**, *98* (14), 146401. https://doi.org/10.1103/PhysRevLett.98.146401.
(60) Kresse, G.; Furthmüller, J. Efficient Iterative Schemes for Ab Initio Total-Energy Calculations Using a Plane-Wave Basis Set. *Phys. Rev. B* **1996**, *54* (16), 11169–11186. https://doi.org/10.1103/PhysRevB.54.11169.
(61) Kresse, G.; Joubert, D. From Ultrasoft Pseudopotentials to the Projector Augmented-Wave Method. *Phys. Rev. B* **1999**, *59* (3), 1758–1775. https://doi.org/10.1103/PhysRevB.59.1758.
(62) Perdew, J. P.; Burke, K.; Ernzerhof, M. Generalized Gradient Approximation Made Simple. *Phys. Rev. Lett.* **1996**, *77* (18), 3865–3868. https://doi.org/10.1103/PhysRevLett.77.3865.
(63) Dudarev, S. L.; Botton, G. A.; Savrasov, S. Y.; Humphreys, C. J.; Sutton, A. P. Electron-Energy-Loss Spectra and the Structural Stability of Nickel Oxide: An LSDA+U Study. *Phys. Rev. B* **1998**, *57* (3), 1505–1509. https://doi.org/10.1103/PhysRevB.57.1505.

(64) Cococcioni, M.; de Gironcoli, S. Linear Response Approach to the Calculation of the Effective Interaction Parameters in the LDA+U Method. *Phys. Rev. B* **2005**, *71* (3), 035105. https://doi.org/10.1103/PhysRevB.71.035105.
(65) Steinmann, S. N.; Corminboeuf, C. Comprehensive Benchmarking of a Density-Dependent Dispersion Correction. *J. Chem. Theory Comput.* **2011**, *7* (11), 3567–3577. https://doi.org/10.1021/ct200602x.
(66) Shang, C.; Liu, Z.-P. Constrained Broyden Minimization Combined with the Dimer Method for Locating Transition State of Complex Reactions. *J. Chem. Theory Comput.* **2010**, *6* (4), 1136–1144. https://doi.org/10.1021/ct9005147.
(67) Shang, C.; Liu, Z.-P. Constrained Broyden Dimer Method with Bias Potential for Exploring Potential Energy Surface of Multistep Reaction Process. *J. Chem. Theory Comput.* **2012**, *8* (7), 2215–2222. https://doi.org/10.1021/ct300250h.
(68) Calle-Vallejo, F. The ABC of Generalized Coordination Numbers and Their Use as a Descriptor in Electrocatalysis. *Adv. Sci.* **2023**, *10* (20), 2207644. https://doi.org/10.1002/advs.202207644.
(69) Baker, T. A.; Xu, B.; Liu, X.; Kaxiras, E.; Friend, C. M. Nature of Oxidation of the Au(111) Surface: Experimental and Theoretical Investigation. *J. Phys. Chem. C* **2009**, *113* (38), 16561–16564. https://doi.org/10.1021/jp9052192.
(70) Hiebel, F.; Montemore, M. M.; Kaxiras, E.; Friend, C. M. Direct Visualization of Quasi-Ordered Oxygen Chain Structures on Au(110)-(1×2). *Surf. Sci.* **2016**, *650*, 5–10. https://doi.org/10.1016/j.susc.2015.09.018.
(71) Xu, F.; Madix, R. J.; Friend, C. M. Spatially Nonuniform Reaction Rates during Selective Oxidation on Gold. *J. Am. Chem. Soc.* **2018**, *140* (38), 12210–12215. https://doi.org/10.1021/jacs.8b07438.
(72) Xu, F.; Montemore, M. M.; O'Connor, C. R.; Muramoto, E.; van Spronsen, M. A.; Madix, R. J.; Friend, C. M. Oxygen Adsorption on Spontaneously Reconstructed Au(511). *Surf. Sci.* **2019**, *679*, 296–303. https://doi.org/10.1016/j.susc.2018.09.012.
(73) Chen, D.; Shang, C.; Liu, Z.-P. Machine-Learning Atomic Simulation for Heterogeneous Catalysis. *Npj Comput. Mater.* **2023**, *9* (1), 2. https://doi.org/10.1038/s41524-022-00959-5.
(74) Zhai, H.; Alexandrova, A. N. Local Fluxionality of Surface-Deposited Cluster Catalysts: The Case of Pt7 on Al_2O_3. *J. Phys. Chem. Lett.* **2018**, *9* (7), 1696–1702. https://doi.org/10.1021/acs.jpclett.8b00379.
(75) Poths, P.; Vargas, S.; Sautet, P.; Alexandrova, A. N. Thermodynamic Equilibrium versus Kinetic Trapping: Thermalization of Cluster Catalyst Ensembles Can Extend Beyond Reaction Time Scales. *ACS Catal.* **2024**, *14* (7), 5403–5415. https://doi.org/10.1021/acscatal.3c06154.
(76) Son, G.; Li, Y.; Shneidman, A. V.; Han, J. H.; Aizenberg, M.; Sautet, P.; Aizenberg, J. Facet-Dependence of Electron Storage in Gold-Decorated Titania Nanocrystals. *Chem. Mater.* **2023**, *35* (22), 9505–9516. https://doi.org/10.1021/acs.chemmater.3c01252.
(77) Masoud, N.; Partsch, T.; de Jong, K. P.; de Jongh, P. E. Thermal Stability of Oxide-Supported Gold Nanoparticles. *Gold Bull.* **2019**, *52* (2), 105–114. https://doi.org/10.1007/s13404-019-00259-9.

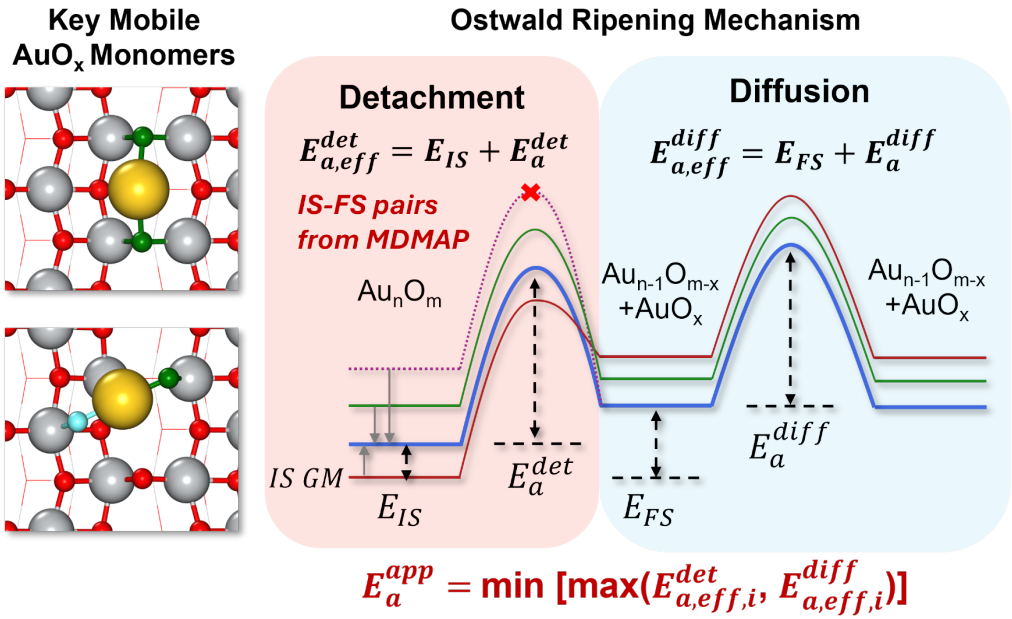

For Table of Contents Only